Marlen Kolbe

SEA LEVEL ANOMALIES IN THE SOUTHERN OCEAN DUE TO THERMOHALINE VARIABILITY

2020

Marlen Kolbe

SEA LEVEL ANOMALIES IN THE SOUTHERN OCEAN DUE TO THERMOHALINE VARIABILITY

Master of Science in Marine and Coastal Systems
Department of Sciences and Technology

Supervised by: Professor Fabien Roquet (University of Gothenburg)
Co-Supervised by: Professor Paulo Relvas (University of Algarve)

2020

THE UNIVERSITY OF ALGARVE

Abstract

Department of Sciences and Technology

Master of Science

by Marlen Kolbe

The Southern Ocean is responsible for the majority of the global oceanic heat uptake. At the same time, higher latitude waters are strongly stratified by salinity. This thesis investigates steric height variability in the Southern Ocean from 2008 to 2017 by analysing potential temperature (θ) and practical salinity (S) profiles obtained from global ocean reanalyses. The work was performed using an innovative method called functional Principal Component Analysis (fPCA). This feature extraction procedure was applied on the θ and S profiles (2000 m depth) which have been transformed into B-spline functions beforehand. The resulting thermohaline modes reveal information about the general θ and S structure, and their variations have been analysed over time. By integrating density anomalies, steric height was computed and related to changes of the modes using a Multiple Linear Regression model. Lastly, steric height trends have been compared to total sea surface height (SSH) data from satellite altimetry.

Despite recent increases in meltwater and atmospheric temperatures, steric height in Antarctic waters above 2000 m has recently dropped due to higher salt content, while subtropical waters farther north have mostly risen due to increased heat storage. Interannual steric height changes are clearly depicted in total SSH variability, but at present the dominant cause for the significant sea level rise south of 30°S is increased freshwater discharge from glaciers and ice sheets.

Keywords: Steric Sea Level; Southern Ocean; Sea Level Variations; Thermohaline Structure; Functional Principal Component Analysis

THE UNIVERSITY OF ALGARVE

Resumo

Department of Sciences and Technology

Master of Science

by Marlen Kolbe

O Oceano Antártico é responsável pela maior parte da absorção global de calor oceânico. Ao mesmo tempo, as águas de latitudes mais altas são fortemente estratificadas por salinidade. Esta tese investiga a variabilidade da altura estérica no Oceano Antártico de 2008 a 2017, analisando a temperatura potencial (θ) e os perfis práticos de salinidade (S) obtidos a partir de reanálises oceânicas globais. O trabalho foi realizado utilizando um método inovador denominado Análise de Componentes Principais Funcionais (fPCA). Este procedimento de extração de características foi aplicado nos perfis θ e S (profundidade de 2000 m) que foram transformados em funções B-spline previamente. Os modos termohalinos resultantes revelam informações sobre a estrutura geral θ e S, e suas variações foram analisadas ao longo do tempo. Ao integrar anomalias de densidade, a altura estérica foi calculada e relacionada às mudanças dos modos usando um modelo de regressão linear múltipla. Por último, as tendências da altura estérica foram comparadas aos dados da altura total da superfície do mar (SSH) da altimetria de satélite.

Apesar dos recentes aumentos na água de degelo e nas temperaturas atmosféricas, a altura estérica nas águas da Antártica acima de 2000 m caiu recentemente devido ao maior conteúdo de sal, enquanto as águas subtropicais mais ao norte aumentaram principalmente devido ao aumento do armazenamento de calor. Mudanças de altura estérica interanual são claramente representadas na variabilidade SSH total, mas no momento a causa dominante para o aumento significativo do nível do mar ao sul de 30°S é o aumento da descarga de água doce das geleiras e mantos de gelo.

Termos chave: Densidade da água do oceano; Oceano Antártico; Variações do nível do mar; Estrutura termohalina; Análise do componente principal funcional

Sumário

O conteúdo de sal e calor da superfície e da camada intermediária do Oceano Antártico aumentou em quase todas as latitudes. A única exceção significativa ocorre no Zona Polar Frontal (PFZ), onde a superfície e a camada intermediária experimentaram um refresco e as águas ficaram menos quentes ou mesmo ligeiramente mais frias quase linearmente. Especialmente logo ao norte do Frente Subtropical (STF; 35°S a 40°S), há uma forte tendência zonal indicando águas mais quentes e salgadas (principalmente devido a um grande aumento em 2010). O antigo resfriamento das águas próximas à Antártica observado em estudos mais antigos não pôde ser identificado. Em vez disso, as águas superficiais de latitudes muito altas estão se aquecendo a uma taxa rápida desde 2014, juntamente com o maior teor de sal. Embora haja disparidades regionais em todas as faixas zonais, a tendência geral aponta para águas subtropicais mais quentes e salgadas, subantárticas mais frias e frescas e águas antárticas mais quentes e salgadas. Embora as temperaturas mais altas ao norte do orrente circumpolar antártica (ACC) representem o aumento do armazenamento de calor oceânico do aquecimento atmosférico, o aumento da salinidade ao sul do ACC é provavelmente devido ao aumento da ressurgência águas profundas do atlântico norte (NADW) como uma resposta à intensificação dos ventos de oeste.

Apesar do fato de que a maioria das regiões do Oceano Antártico estavam sujeitas a temperaturas mais altas, a contribuição termostérica foi parcialmente compensada por um aumento na salinidade. Embora, globalmente, a variabilidade da altura estérica seja amplamente controlada apenas pela temperatura, as mudanças de salinidade no Oceano Antártico amorteceram o efeito do aquecimento ao sul do frente polar (PF). Isso se deve ao fato de que nas partes mais meridionais do Oceano Antártico, a salinidade domina a estratificação do oceano. Mesmo na região subtropical, ela desempenha um papel significativo: a purificação das águas intermediárias nas proximidades da corrente do Peru no Pacífico Sul contrabalançou a tendência negativa da altura estérica causada pelas águas mais frias.
No geral, a temperatura está claramente dominando a estrutura atual e a altura estérica média das águas subtropicais e ainda responsável pela tendência positiva da altura estérica devido ao armazenamento de calor.

Pode-se concluir que, em média, a temperatura domina a variabilidade da altura estérica ao norte do PF, enquanto as mudanças de salinidade desempenham um papel vital ao sul do PF. Como consequência de um aumento geral nas temperaturas e salinidade, a altura estérica aumentou nas águas subtropicais do Oceano Antártico e caiu mais perto da costa Antártica.

Mudanças de altura estérica no Oceano Antártico estão afetando significativamente o variações do nível do mar (SLV) total, especialmente intra-anual. Em escalas de tempo mais longas, o rápido aumento do nível total do mar no Oceano Antártico é causado principalmente por processos baristáticos. De 2008 a 2017, apenas 7% do subida do nível do mar (SLR) total se originou de fluxos de calor e água doce. A entrada de massa consistente ao longo da década investigada reverteu a queda do nível do mar estérico perto da costa da Antártica e contribuiu para a SLR estérica em águas subtropicais do Oceano Antártico.
Enquanto os níveis de altura estérica definem as variações intra-anuais e a distribuição média do SSH total sobre o Oceano Antártico, o recente aumento decadal (2008 a 2017) foi causado predominantemente por mudanças no orçamento global de água. É muito provável que o aumento da temperatura atmosférica nas décadas seguintes acelere o nível do mar estérico e baristático no Oceano Antártico.

Declaration of Authorship

I, Marlen Kolbe, declare that this thesis titled 'Sea Level Anomalies in the Southern Ocean due to Thermohaline Variability' and the work presented in it are my own. I confirm that:

- The thesis comprises only my original work towards the Master of Science; and
- due acknowledgement has been made in the text to all other material used.

Signed: 

Date: *29.09.2020*

Contents

List of Figures

List of Tables

Abbreviations

AABW	Antarctic Bottom Water
ACC	Antarctic Circumpolar Current
AR5	5^{th} IPCC Assessment Report
cm	Centimeter
EOF	Empirical Orthogonal Functions
EOS	Equation Of Seawater
fPCA	Functional Principal Component Analysis
GMSL	Global Mean Sea Level
GREP	Global Reanalysis Ensemble Product
GSLV	Global Sea Level Variations
GSW	Gibbs Sea Water
IPCC	Intergovernmental Panel on Climate Change
m	Meter
mm	Millimeter
MOC	Meridional Overturning Circulation
MLR	Multiple Linear Regression
NADW	North Atlantic Deep Water
PC	Principal Component
PF	Polar Front
PCA	Principal Component Analysis
psu	Practical Salinity Unit
RCP	Representative Concentration Pathway
RMSE	Root Mean Square Error
RSLV	Regional Sea Level Variations
$\mathbf{R^2}$	R-squared

S	Practical Salinity
SACCF	Southern Antarctic Circumpolar Front
SAF	Subantarctic Front
SAM	Southern Annular Mode
SAZ	Subantarctic Zone
SBdy	Southern Boundary of the Antarctic Circumpolar Current
S-EOS	Simplified Equation Of Seawater
SLV	Sea Level Variation
SLR	Sea Level Rise
SSH	Sea Surface Height
SSS	Sea Surface Salinity
SST	Sea Surface Temperature
STF	Subtropical Front
TEOS	Thermodynamic Equation Of Seawater
yr	Year

Symbols

hPa	hectoPascal	SI Unit (10^2 N/m^2)
p	Pressure	dbar
z	Depth	m
η	Steric Height	cm
θ	Potential Temperature	°C
ϱ	Density	kg/m^3
ξ_l	Eigenfunction (Vertical Mode) of the lth Mode	Unitless

Chapter 1

OBJECTIVE AND SCOPE

1.1 Motivation

As climate change continues to be of serious concern globally, there is increased interest to study and predict climate-related sea level change. The effect of rising temperatures and swings in weather patterns have so far led to major changes in ocean properties and a significant increase in the rate of global mean sea level (GMSL) rise (Collins et al., 2010; Church et al., 2013). From 1993 to 2017, the average rate of GMSL rise due to climate change was estimated to have been 2.9 mm/yr, with a simultaneous acceleration of 0.084 ± 0.025 mm/yr^2 (Nerem et al., 2018).
One apparent and often discussed cause of sea level rise (SLR) is the melting of land ice (glaciers and ice sheets). Due to the acceleration of land ice melting, the so-called barystatic component (changes in the ocean's mass) has contributed the most to the GMSL rise in recent years (Kim et al., 2019).

Thermal expansion (the fractional change in volume of any water column in response to an increase in temperature) used to be the primary cause of rising sea levels and still is the dominant contributor if glaciers and ice sheets were treated separately (Church et al., 2013; Griggs et al., 2017). For lack of qualitative or quantitative data, and sufficient understanding of physical processes, estimating accurate contributions from both barystatic and non-barystatic sources remains a scientific challenge (Church et al., 2013).

The Southern Ocean in this context is of major interest. According to a recent study based on observations from 2006 to 2013, it has contributed 67% to 98% to the change in global heat content of

the 0 – 2000 m water column (Llovel and Terray, 2016). However especially in the southernmost waters there still is insufficient understanding of heat transfer processes and regional sea level responses. The global role of the Southern Ocean is considered to be vitally important, yet due to sparse data and complex features, it remains one of the most understudied oceans. Recent additions of qualitative data facilitate the understanding of its structure and responses to the changing climate, and scientists stress the necessity to analyze the Southern Ocean in terms of changes in physical properties for more accurate model outputs (Hallberg et al., 2013; Riser et al., 2016; Zhang et al., 2019; Skinner et al., 2020).
This thesis aims to contribute to a better understanding of how temperature and salinity changes effect the steric sea level in the Southern Ocean.

1.2 Objectives

The present study investigates the steric component of sea level changes in the Southern Ocean by analyzing how sea surface height (SSH) anomalies can be related to the variability of thermohaline modes. The general objective is to find out how and where temperature and salinity anomalies have affected steric height variability in the Southern Ocean from 2008-2017.

The three specific questions this thesis addresses are:

1) How did the temperature and salinity structure of the Southern Ocean change from 2008 to 2017?
2) Where is steric height variability in the Southern Ocean dominated by temperature and where by salinity on different spatial-temporal scales?
3) How much do these dynamic changes affect total SSH variability in the Southern Ocean?

The focus of the present study lies in investigating causes and trends of regional steric height. Therefore the first and the second objective are of primary importance. The third objective puts the results into context and refers back to the motivation behind this study, but is of minor priority.

1.3 Study Area

The study area comprises the complete region of the Southern Ocean, as well as the southernmost water masses of the Indian, the Pacific and the Atlantic Ocean that adjoin and interact with waters

of the Southern Ocean (Figure 1.1).

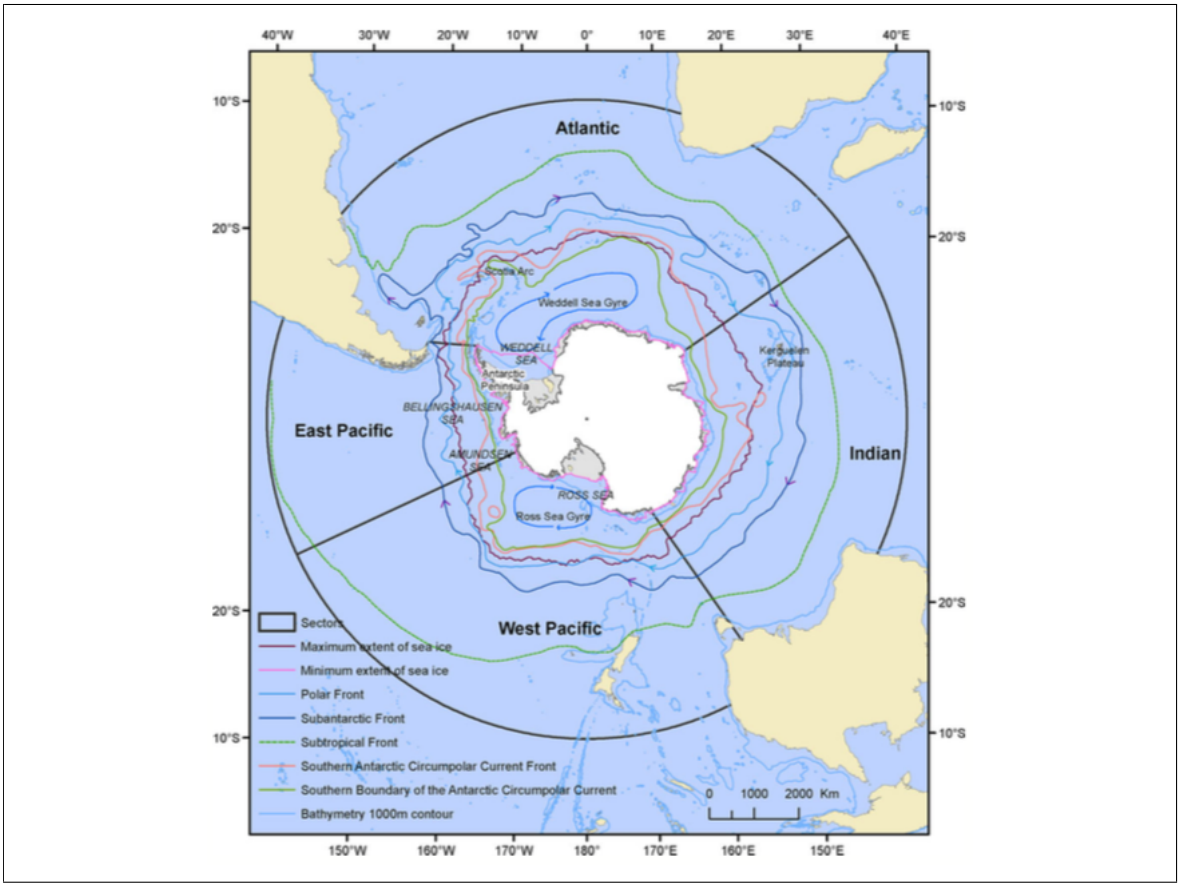

FIGURE (1.1) Map of the Southern Ocean divided into ocean sectors, showing the main fronts along with the Ross and Weddell Sea Gyre systems, the maximum and minimum sea ice extent and the 1000 m bathymetry contour. Source: Constable et al., 2014.

Following most scientific literature, the northern boundary of the Southern Ocean is defined by the Subtropical Front (STF). This front is of great interest regarding dynamic changes, as it represents the sharp transition from warm and salty to colder and fresher surface waters (Orsi et al., 1995; Belkin and Gordon, 1996; Pauthenet et al., 2017). All water masses south of the STF are officially considered as parts of the Southern Ocean. Along with this northern boundary, Figure 1.1 features the Subantarctic Front (SAF), the Polar Front (PF), the Southern Antarctic Circumpolar Front (SACCF) and the Southern Boundary of the Antarctic Circumpolar Current (SBdy). All of these fronts have an important role regarding their influence on global ocean physical and biogeochemical exchanges (Rintoul and Sokolov, 2001; Pauthenet et al., 2017). Together they form the Antarctic Circumpolar

Current (ACC). It is characterized by an eastward flow that moves all around the Antarctic continent and represents the largest wind-driven current on earth (Donohue et al., 2016).

Strictly speaking, the study domain covers all water masses (above 2000 m below mean sea level) in the Southern Ocean, and additionally those north of the STF, but south of 30°S. In the following the term 'Southern Ocean' is used to refer to the entire study domain.

Chapter 2

INTRODUCTION

2.1 Global and Regional Sea Level Variations

This chapter covers the respective causes to SSH and steric height variability from a temporal and a spatial perspective.
The present study uses the term 'sea level' (and 'SSH') in a relative sense as the measurement of the ocean surface referenced to the geoid. This means that SLV are only dependent on changes of the ocean itself. A possible change of the geoid's shape (e.g. due to mass redistribution) during the investigated time period can be considered to be very minimal and is therefore neglected here.

On a global scale, sea levels show a long-term rise as a cause of either thermal expansion and/or mass input from land sources. Correspondingly, long-term fall of global sea level can be explained by thermal contraction and/or a decrease in ocean mass as a result of increased land water storage. Those effects, steric and barystatic, account for variations in the total global sea level variations (GSLV) as shown in Equation 2.1 (adapted from García et al., 2006):

$$GSLV_{\text{total}} = SLV_{\text{steric}} + SLV_{\text{mass}} \tag{2.1}$$

Investigations in GMSL are usually conducted in the context of changes over longer time scales such as past and present climate change.

On shorter timescales and from a regional perspective, there are further motives to study SLV. On top of steric and mass-related components affecting SSH changes, unadjusted regional SLV additionally depend on local effects most of which can not be identified in global SLV. Equation 2.2 classifies the contributors to regional SLV, where these additional factors are included. Stammer and Cazenave (2017) have noted that on top of steric and barystatic contributions, regional total sea level variations (RSLV) are further produced by atmospheric loading variations as well as 'static terms':

$$RSLV = SLV_{\text{steric}} + SLV_{\text{mass}} + Atmospheric\,Loading + Static\ Terms \tag{2.2}$$

The local atmospheric loading has an inverse barometric effect on sea level: Any increase in atmospheric pressure lowers the sea level. Similarly, high atmospheric pressure conditions are associated with positive SSH anomalies (Pond and Pickard, 1983). Latitudes are of particular importance regarding this forcing, as changes in atmospheric pressure are more regular at higher latitudes (Iz et al., 2018). Additionally, the effect on SLV is greater at high latitudes (2-3 cm) compared to the tropics (<1 cm), if investigated on annual or longer timescales (Ponte, 2006; Stammer et al., 2013).
Besides, regional SLV can partly occur due to aftereffects of present-day mass distributions of the earth or glacial isostatic adjustment, both of which are herein referred to as 'Static Terms' (Milne et al., 2009; Tamisiea and Mitrovica, 2011; Stammer and Cazenave, 2017).
Although the regional SLV equation from Stammer and Cazenave (2017) terms the steric and barystatic SLV before 'Atmospheric Loading' and 'Static Terms', this should not be misinterpreted as an indicator for their proportional value to SLV. Previous studies have shown that RSLV contributions are significantly dependent on the exact location (Halliwell and Allen, 1984; Fukumori et al., 1998; Tsimplis et al., 2008), as well as on the season if analysed on an intra-annual time scale (Gomis et al., 2008; Dangendorf et al., 2013). It should therefore be stressed that Equation 2.2 addresses the encompassing non-tidal variability of sea level, where the summands are not (and can not be) ordered according to their universal contribution.

2.2 Steric Sea Level and the Southern Ocean

The classification of steric height (η) in the context of SLV requires the introduction of density anomalies. Similar to atmospheric density, the density of the ocean depends on potential temperature (θ), practical salinity (S), and pressure (p) changes. Potential temperature refers to the temperature a water parcel reaches if brought up to the surface from its original position adiabatically. In the present

study, the old standard Equation Of Seawater (EOS-80) is adopted to define the equation of state, because the utilized model data follows this standard. Although using the new standard Thermodynamic Equation Of Seawater (TEOS-10) would have been preferred (making density a function of conservative temperature and absolute salinity), results are not significantly impacted by the choice of the standard (Fabien Roquet, personal communication).
Steric height anomaly is obtained by vertically integrating density anomalies. The surface steric height relative to a reference level $z = -h$ is given as

$$\eta = -\frac{1}{\varrho_0} \int_{-h}^{0} \left[\varrho \left(\theta, S, p = \varrho_0 g z \right) - \varrho_{ref} \left(p = \varrho_0 g z \right) \right] \, dz, \tag{2.3}$$

where ϱ represents seawater density, ϱ_0 a constant reference to seawater density, g the gravitational constant, ϱ_{ref} the density for a standard seawater composition with $\theta_{ref} = 0^o C$ and $S_{ref} = 35$ psu, and pressure p is evaluated using the Boussinesq approximation.

As its name suggests, thermal expansion has a negative relation with density and a positive effect on sea level, i.e. lowering density and increasing sea level height. An increase in salinity produces the opposite effect: Density increases and therefore sea level drops. The respective effect of θ and S on steric height anomalies is called thermosteric (η_θ) and halosteric (η_S) effect. Here, the negative density anomaly is integrated from the surface ($\eta = 0$) to the reference level ($\eta - h$). $\theta^\star$ and S* refer to θ and S as a constant averaged over time (Storto et al., 2019a).

$$\eta = \eta_\theta + \eta_S = -\frac{1}{\varrho_0} \int_{\eta=-h}^{\eta=0} \delta\varrho \left(\theta, S^\star \right) dz - \frac{1}{\varrho_0} \int_{\eta=-h}^{\eta=0} \delta\varrho \left(\theta^\star, S \right) dz. \tag{2.4}$$

As briefly mentioned, changes in steric height can occur on all time scales, due to its sole dependence on temperature and salinity changes. Apart from the challenging aspect of determining the relative steric height of ocean water, it is also difficult to define whether variations in steric height are primarily driven by salinity or temperature. This is due to the fact that the effect of changes in temperature and salinity on the steric height can compensate each other. At the same time, it is a problem to determine where exactly in the water column these physical properties have changed and for how long they will remain (Frölicher et al., 2015; Pauthenet et al., 2017).

It is certain that the additional heat of the climate system due to greenhouse gases is almost entirely absorbed by the ocean (93% over the last 50 years), which is leading to an overall expansion of the ocean's water masses. Thermal expansion has dominated the effect of mass-induced SLR on a global

scale up until recently (Wijfells et al., 2016; da Gama et al., 2020).
Although seawater density is a function of both salinity and temperature, studies discussing or estimating future steric sea level changes often focus on the thermosteric contribution only. This is justified by the fact that in most regions, the salinity-induced (halosteric) contribution is considered to be almost negligible (Church et al., 2013; Storto et al., 2019a).

Figure 2.1 shows the latest predictions of the second highest Representative Concentration Pathway (RCP) 6.0 of the fifth IPCC Assessment Report (AR5), predicting that the thermosteric component will likely remain one of the greatest contributors until the end of this century, closely followed by the combined melt water from terrestrial glaciers, and the Greenland and Antarctic ice sheets. Depending on the particular IPCC scenario, thermal expansion will account for 30% to 55% of the 21^{st} century GMSL rise in future predictions of the AR5 (IPCC, 2013).

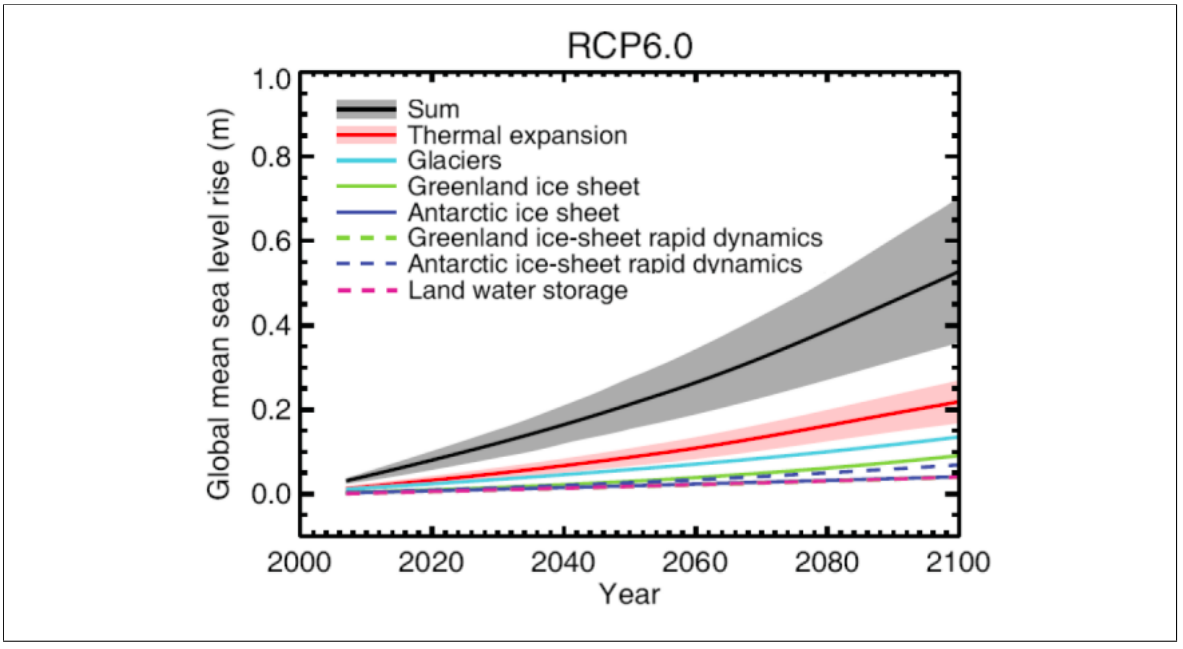

FIGURE (2.1) Predicted contributions to SLR by source in the RCP 6.0 scenario of the IPCC 5th Assessment Report. Source: AR5, IPCC, 2013.

The increase in Southern Ocean heat uptake over the last four decades did not result in a uniform distribution of increased ocean temperature. Instead, only waters north of the ACC and especially at the surface have showed significant warming, whilst south of the ACC scientists have found only very little warming so far. Although this delayed effect close to the coast had already been detected by earlier studies, there is no scientific consensus regarding the actual cause(s) for this observation

(Goosse et al., 2014; Li et al., 2013; Sallée et al., 2013).

Armour et al. (2016) have recently delivered a well-founded explanation and overview of the different factors. The authors have found that the dominant cause for this delayed warming trend lies in the dynamics of the meridional overturning circulation (MOC): Although the vast majority of oceanic heat uptake occurs in the higher latitudes of the Southern Ocean, the southernmost areas simultaneously present those with the least amount of heat stored. The authors have concluded that instead of heat being stored locally, the residual mean flow (upwelling waters along the ACC flowing equatorward) transports the absorbed heat to waters farther north. Following previous studies, Armour et al. (2016) have further noted that the strengthening of winds has enhanced upwelling of colder water close to the Antarctic coast, which has contributed to past and present cooling of high-latitude waters. Other explanations include a meltwater-induced freshening of waters close to Antarctica, preventing the cold water to mix and sink, as well as increased sea ice cover and wind-induced sea spray shielding radiation. The authors have stressed that especially the strengthening of winds has previously contributed to the cooling of the southernmost waters, but are playing a minor role in present and future changes. Indeed the ozone hole over Antarctica, which has been found to be responsible for this shift in winds, is currently recovering (Banerjee et al., 2020). Along with the surface freshening and a decrease in radiative forcing, these effects have been characterized as secondary causes contributing to the delay of ocean warming near Antarctica. With the MOC being considered as the primary cause, the authors further predict that over the next decades, the upwelling waters close to Antarctica will store some of the excess heat, which would eventually result in higher ocean temperatures even south of the ACC (Armour et al., 2016).

Still, there is a large uncertainty in the exact amount of ocean heat changes, which is primarily a result of poor data availability in this relatively remote area of the ocean, where both salinity and temperature data products have so far been scarce due to undersampling (Ishii et al., 2006; Frölicher et al., 2015; Pauthenet et al., 2017; Newman et al., 2019).

Regarding the relative steric contribution to the total sea level, another recently published study from Storto et al. (2019a) has found that the Southern Ocean is again of particular importance; About 50% to 60% of the total SSH change rate from 1993 to 2015 arose from rising steric sea levels. Only in the Atlantic Ocean the steric contribution to SLR was found to be similarly high, while in the Pacific and Indian Ocean the contribution is lower, with a SSH change rate of only 20% to 40% (Storto et al., 2019a).

Chapter 3

METHODOLOGY

This chapter provides a generic overview of the applied methods in order to allow for a reproduction with similar oceanographic datasets. While most methods can be applied to a variety of data from various scientific fields, the following descriptions are targeted towards the use of θ and S profiles as a function of depth, time and space.

For this study, θ and S profiles have been normalized into B-spline functions, which allows to apply a functional approach on the splines to obtain Principal Components (PCs). The PCs are the basis of this study, along with the steric height data. The latter was calculated using the unmodified θ and S profile data as described below. Both variables have been analysed over time from a global, zonal and regional view. Their relation has further been discussed with the help of a Multiple Linear Regression (MLR) model. Lastly the results have been compared to total SSH observations from altimetry data. Each process is described in more detail below.

All computations and visualizations were made using the Python programming language.

3.1 B-spline Decomposition

As a first step in order to reduce the amount of data points and create a basis for the upcoming analysis, the θ and S profiles have been decomposed into continuous B-spline functions. This step is not only necessary for reduce the computational load, but further helps to simulate the functional depth-related behaviour of most oceanographic variables. B-splines are generalized functions of the

Bézier curve (Weisstein, 2009), and are commonly used if the goal is to replace a large amount of data points with smooth functions that can accurately imitate these points. The amount of internal knots (K) define the smoothness (and thus the accuracy) of the curves and should be adjusted to the specific dataset. The profiles then consist of K coefficients each and can be compared to each other at any depth (Pauthenet et al., 2017).
The code describing such a profile decomposition into B-splines is available on GitHub for R environments (https://github.com/EPauthenet/fda.oce) and has also been translated into the Python language
(https://github.com/EPauthenet/fda_oce_python/blob/master/fda_oce_python.ipynb).

3.2 Functional Principal Component Analysis

While there is frequent use of the standard Principal Component Analysis (PCA) or the Empirical Orthogonal Functions (EOF) approach within the scientific community since several decades, the concept of a functional PCA (fPCA) has only been defined and gained attention since around the start of this century (Ramsay and Silverman, 2005). Similarly to the standard version, the aim of it lies in dimensionality reduction and feature extraction. The way it differs from standard PCA is that it is not directly applied on discrete values, but can be applied on functions (Pauthenet et al., 2017).

The result of the fPCA are modes and corresponding PCs. The modes are the eigenfunctions and the PCs are the respective coefficients of the modes. Here the PCs virtually replace the original θ and S values by maximizing the amount of explained variance. Similar to the above explained choice of internal knots for the spline decomposition, the total number of PCs can be selected depending on how much of the variance the resulting modes cover and how many variables are desired to be investigated. The justification for this variable transformation further lies in dimension reduction (as the θ and S data so far is still a function of the K=20 B-spline coefficients), and in the dynamic nature of the θ and S structure. The fPCA further provides a set of uncorrelated variables (PCs) and allows for a quantification of the explained variance that θ and S induce on the water column (Ramsay, 2004; Viviani et al., 2005; Pauthenet et al., 2017). The time- and space-dependent PC variables are then explaining the behaviour of the water columns with changing depth with a single value, instead of being a function of multiple fixed depth points. The potential θ and S profile at any depth z can then be reconstructed as

$$\theta(z) = \bar{\theta}_0(z) + \sum_{i=1}^{N} PC_i \xi_l(z) \tag{3.1}$$

and

$$S(z) = \bar{S}_0(z) + \sum_{i=1}^{N} PC_i \xi_l(z) \tag{3.2}$$

respectively. Here $\bar{\theta}_0$ and $\bar{S}_0$ represent the mean reference θ and S profiles and ξ_l represents the added eigenfunctions of θ and S. With $l < N$, N represents the number of modes and defines the order of truncation.

For the present study the fPCA was applied on the monthly climatology of the θ and S data, which has previously been computed as the mean of each month throughout the time period (2008-2017). This basis has then been used to project all of the monthly mean profiles, resulting in a single value for each of the PCs for each profile. Another example with a profound explanation of this method can be found in a paper, where applications of the PC results are described in detail and exemplified by a relation of the modes to the Southern Ocean frontal structure (Pauthenet et al., 2017).

3.3 Calculation of Steric Height

The steric height of any oceanographic profile of θ and S values can be calculated using the *geo_strf_dyn_height()* function from the Python implementation of The Gibbs SeaWater (GSW) Oceanographic Toolbox (available on Github: https://github.com/TEOS-10/python-gsw). Temperature and salinity profile data can be introduced into the function *gsw.geo_strf_dyn_height(SA,CT,p,p_ref)*/9.7963, where SA represents the salinity vector, CT represents the temperature vector, and p the vector containing the depth in meters. p_ref should be set to the maximum depth corresponding to the previous vectors. This study assumes that the majority of steric height changes occurs within the first 2000 m and hence restricts the θ and S profiles to the provided depth values until 2000 m. The function, divided by the constant value of gravitational acceleration (9.7963), then returns the steric height values for each spatial and temporal point of the data cloud. The values are returned in meters relative to the reference level. For this study the outputs have been zero-centered as well converted into cm for presentation and comparison purposes.

3.4 Time Series and Zonal Analysis

The steric height, the first three PCs (using the knowledge about how the θ and S structure changes with higher and lower PC values), and the SSH data have been analyzed on a spatial and temporal scale.

First each of the three time series has been decomposed after a moving average method of the Python 'Statsmodels' module. The present study is primarily focused on the trend components. The decomposition provides fluctuating trendlines instead of linear slopes. Linear trends have then been computed for the mean time series of the entire domain, as well as for all latitudes separately, with the polyfit function of Python's 'Numpy' module. This function returns the coefficients minimizing the squared error of any polynomial function, in this case of degree 1.

3.5 Multiple Linear Regression Analysis

The PC values of each grid point store information about changes of the θ and S structure and have been analyzed in regard to their relation with SLV.
This has been performed with a Multiple Linear Regression (MLR) model, where the steric contribution to sea level is predicted by the PC values. Alternatively, the model could be trained using altimetry-based observations of SSH, but this would not be optimal for a direct comparison to the effect of θ and S changes, since there are other factors that can drive multi-annual SSH variability (especially the barystatic component).
Here, the MLR model serves as a basis to analyze where changes in θ and S (in form of the PCs) drive variations of the steric component only. A standard description of such a regression model can be represented by equation 3.3:

$$\eta_{\mathrm{i}} = \beta_0 + \beta_1 x_{\mathrm{i},1} + \beta_2 x_{\mathrm{i},2} + \cdots + \beta_{\mathrm{k}} x_{\mathrm{i,k}} + \epsilon_{\mathrm{i}}. \tag{3.3}$$

For both the dependent variable η and the independent variables (x), the subscript i here represents a single grid point of one month. β refers to the estimated regression coefficients minimizing the sum of squared errors, k is the amount of independent variables (here modes), and ϵ is the error term. β_0 is the intercept, which is zero if the dependent dataset (here steric height) is zero-centered.

The MLR model has been used to relate the θ and S information contained in the modes to the steric height, as described in chapter 2.4. An adapted version of Equation 3.3 to one that describes the used dataset can be presented as

$$\eta_{\mathrm{x,y,t}} = a_1 PC1_{\mathrm{x,y,t}} + a_2 PC2_{\mathrm{x,y,t}} + a_3 PC3_{\mathrm{x,y,t}} + a_4 PC4_{\mathrm{x,y,t}} + a_5 PC5_{\mathrm{x,y,t}}, \tag{3.4}$$

with x,y and t representing latitude, longitude and time respectively. The resulting regression coefficients are discussed in chapter 5.4.

The regression analysis is complemented by a correlation analysis to understand the relation of the first two modes in different sectors. All correlation coefficients have been computed after the Pearson correlation type using the $corr()$ function provided by the Python Pandas series.

3.6 Comparison to Satellite Data

In order to investigate the third objective (comparing the steric sea level to the total sea level), a dataset of SSH covering the same time period and spatial area is needed. Many ocean reanalysis products provide θ, S and SSH data globally, which makes it easy to replicate the following investigations with other regions and/or other data providers. In this study investigations of how much of the total SLV in the Southern Ocean can be explained by steric height changes is mainly based on visual analyses and simple calculations.

Chapter 4

CASE STUDY

4.1 Data Sources

The analyses of this project are based on data obtained from the 'GLOBAL-REANALYSIS-PHY-001-031' product provided by the Copernicus Marine Environment Monitoring Service. This reanalysis is an ensemble product of the four reanalyses 'GLORYS2V4' from Mercator Ocean, 'ORAS5' from ECMWF, 'GloSea5' from Met Office, and 'C-GLORS05' from CMCC.
Data from this Global Reanalysis Ensemble Product (GREP) has so far shown very good performance in the comparison to observations and has been found to be very suitable for steric height studies (Storto et al., 2019b; de Souza, 2020). GREP is also one of the few ocean reanalysis products that is being updated frequently, providing information on various ocean variables in daily and monthly format from 1993 until 2017 (as of now).

The data was assembled from a numerical model and is freely available in NetCDF-4 format. All extracted variables for this project constitute monthly mean averages from 2008 to 2017. The horizontal resolution of the grid is 0.25° and the total grid size is 1440*681, which has been reduced to 1440*200 for the domain of this study. Out of these grid points, only every second latitude and longitude value has been extracted to reduce the computational load and to avoid spatial auto-correlation. The three variables for this project extracted from GREP are sea surface height (SSH) as well as θ and S profiles. The two latter variables are provided as a function of depth and are available from the sea surface to the bottom of the ocean (typically found at 6000 m below sea level in abyssal plain regions). Analogous to previous steric height studies and due to poor spatial coverage of deep hydrographic observations,

the θ and S data have been restricted to a maximum depth of 2000 m, where the vast majority of thermo- and halosteric height change take place (Sokolov et al., 2009; Sutton and Roemmich, 2011; Levitus et al., 2012, Gaillard et al., 2016; Storto et al., 2019a). Still it should be noted that steric height studies (especially if compared to total SSH) would result in slightly lower uncertainties if the data was reliable enough to allow for a full- water column calculation of steric height.

4.2 Data Transformation

The θ and S profiles have been decomposed into continuous B-spline functions. Here, each θ and S profile has been decomposed into 20 B-spline functions. For each of the horizontal stations (720*100 - NaN areas), the information could therefore be reduced from 2*54 values per profile (54 depth levels for both θ and S) to 2*20 eigenfunctions per profile. Figure 4.1 illustrates how the B-splines fit on two exemplary profiles:

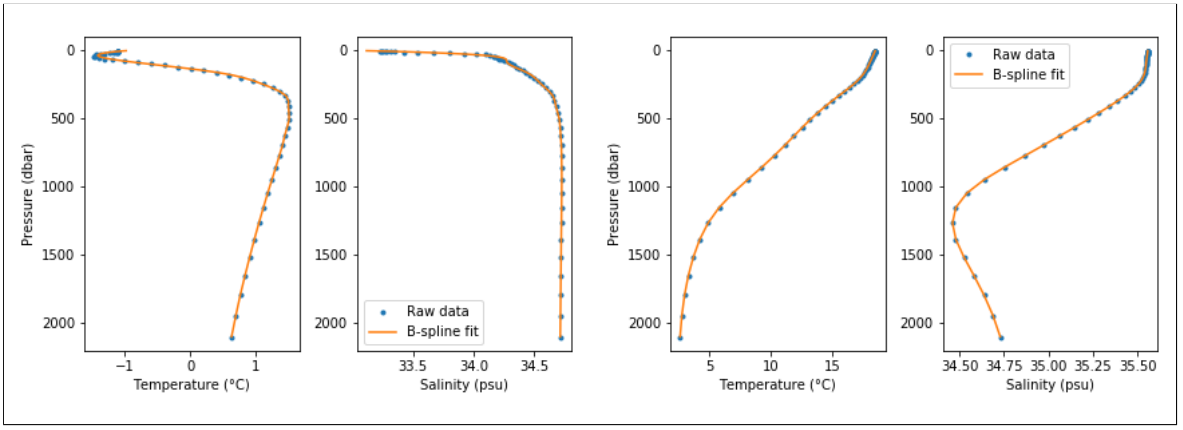

FIGURE (4.1) B-spline fit with 20 segments on two different θ and S profiles (left: Profile #150; right: Profile #500,000.

As generally described in chapter 3.2, a fPCA was applied on the θ and S profiles to determine the PCs that explain the most dominant and characteristic θ and S changes with depth. Instead of applying the fPCA on all θ and S values of the 54 depth levels, here it has been applied on the coefficients of the B-spline functions. For this study the modes have been computed on the monthly averages of the extracted data from 2008 to 2017.

As the first five modes already explain almost 99% of the total variance, only the effects of the first five modes are presented in the following. The focus lies on the first three modes (explaining almost

97% of the total variance), which have been analyzed with regard to their information on the water column structure as well as their effect on steric height.

4.3 Data Overview

The steric height data has been computed, converted into cm and centered around zero as described in chapter 3.4. As the θ and S profiles of the GLORYS model used for this study consist of 720*100*120 = 8,640,000 - NaN areas = 6,090,240 data points each (without dimension z), there are as many data points (6,090,240) for steric height as there are for PC_i.
The SSH data is based on satellite observations and has a slightly greater coverage (mostly due to more data points closer to the islands and continents), with a total number of 6,875,280 values (again every fourth grid point) that have also been centered around 0 and converted into cm. For the comparison analysis to steric height, only the same grid points have been considered.

Table 4.1 provides a statistical overview of all main variables.

	PC1	PC2	PC3	Steric Height	SSH
#	6,090,240	6,090,240	6,090,240	6,090,240	6,875,280
std	1.224	0.617	0.261	61.919	78.499
min	-1.645	-1.237	-1.149	-96.345	-132.147
25%	-1.062	-0.594	-0.148	-64.258	-83.378
50%	-0.475	0.033	0.029	6.664	5.883
75%	0.942	0.595	0.161	59.277	77.182
max	3.690	1.560	1.323	160.037	184.866

TABLE (4.1) Total number of values (#), standard deviation (std), minimum (min), maximum (max), and quantiles (25%, 50% and 75%) of all zero-centered spatio-temporal values of the first three modes as well as the steric height and the SSH dataset.

Chapter 5

RESULTS AND DISCUSSION

This chapter presents and discusses the decomposition of the main modes and their effect on steric height, featured by a tempo-spatial analysis. The main focus is set on non-seasonal variability, as seasonal changes in sea level and physical properties of the Southern Ocean are covered relatively well in the recent literature (Wu et al., 2011, Pellichero et al., 2017; Armitage et al., 2018). They are also less clear indicators of climatic changes. Although time series of ten years do not serve as reliable climate change indicators, they can capture important processes that can be overlooked on longer timescales. Especially in dynamic regions, such as the Southern Ocean, climatic responses are complex and less linear.

5.1 Thermohaline Modes and their Relation to Steric Height

The resulting five modes, computed by using the annual average of the monthly climatology, combined explain 98.69% of the θ and S variance. PC1 alone already contains 74.46% of the θ and S variability. The added percentage of explained variance for the higher modes decreases largely with each added mode. PC2 explains 18.83% of the averaged θ and S changes, resulting in a combined explained variance of 93.29% of PC1 and PC2 together. The remaining modes PC3, PC4 and PC5 add 3.28%, 1.47%, and 0.65% respectively.

In addition the total variance each mode induces on the water profiles, the utilized fPCA functions also provide the relative fraction of variance θ and S explain on each mode. For example, in the case of PC1, temperature plays a greater role (60%) than salinity (40%) on the effect. In order to evaluate the resulting PC values of each mode for the grid points, it is necessary to first analyze their meaning by determining the information contained with higher and lower PC values. Each of the five modes conveys information about how θ and S changes with depth. For the purpose of interpreting what

higher or lower PC_i values reveal about the vertical structure of the water columns, the eigenfunctions ξ_l^θ and ξ_l^S with $l \in \{1,...,20\}$, as calculated by the fPCA, have been added and subtracted to the mean profiles of the modes.

Figure 5.1 illustrates those effects on the first three modes (see Figure A.1 for information contained in the fourth and the fifth mode).

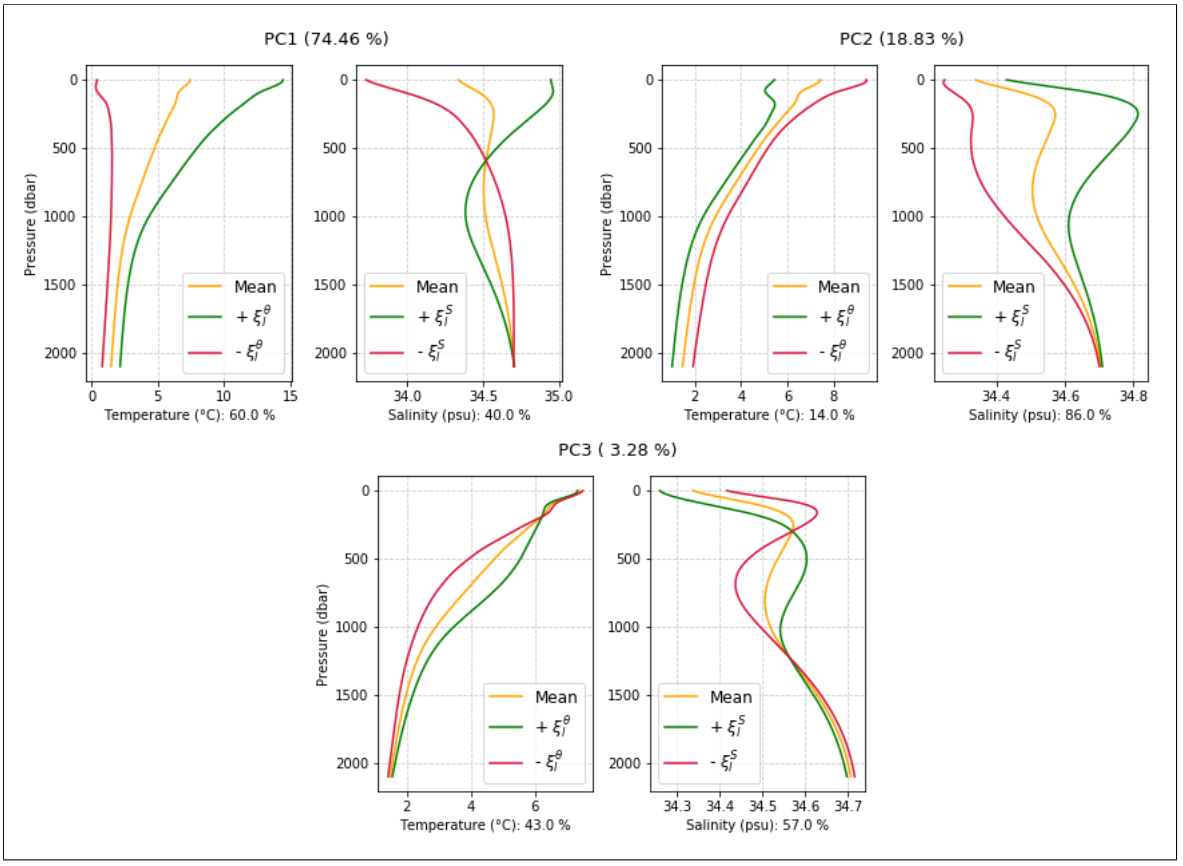

FIGURE (5.1) Effect of adding (green curves) and subtracting (red curves) the eigenfunctions of the mean profiles (yellow curves) computed from the climatology basis.

The first mode accounts for 74.46% of the total variance, meaning it greatly dominates most θ and S changes in the domain. The plotted curves in the upper left panel of Figure 5.1 reveal that a higher PC1 value represents warmer surface waters for the whole water column (0 to 2000 m), but for the surface waters in particular. A lower PC1 value, as represented by the red curve, implies that the temperature is more likely to remain the same with depth and is significantly colder. As for the salinity aspect, higher PC1 values indicate saltier surface waters (up to 35 psu), while a lower value can lower salinity to almost 33.5 psu at the surface. Further, at around 600 meters below the surface,

there is an inversion, meaning that at the intermediate water level salinity drops with a higher PC1 value, and increases with a lower PC1 value. As temperature is slightly dominant for the first mode, any changes in PC1 are more likely to be induced by a change in temperature.
Knowing that density decreases with higher temperatures, it can then be expected that an increase in PC1 is related to an increase in steric height. Due to the dominance of θ this would be accurate even if there was a simultaneous increase in salinity (which lowers steric height) over the whole water column. The lack of such a uniform increase or decrease in salinity contributes to the conclusion that density changes due to variations of the first mode are mainly caused by temperature variability.

A large part of the remaining variance (18.83%) can be explained by changes of the second mode. Here, the relative contribution of temperature and salinity has greater meaning compared to the first mode. With only 14% of the variance being explained by temperature changes, salinity plays the essential role for changes of the second mode. A higher PC2 value indicates more saline waters and a lower PC2 value indicates fresher waters. This is valid for the entire water column, but is more pronounced in the intermediate waters. Regarding temperature, the effect of adding and subtracting the eigenfunction is mainly impacting the surface waters, with lower temperatures being related to higher PC2 values and vice versa.
Due to both the decrease in temperature and especially the increase in salinity that a higher PC2 value entails, it is certain that any increase in PC2 has a negative effect on steric height.

PC3 explains only 3.28% of the variance and shows the smallest deviations of both θ and S from the mean profile (see different scaling of the x-axis, whose range almost linearly decreases from PC1 to PC3). While the addition or subtraction of the third eigenfunction does not distinctly warm or cool the surface layer, there is a clear warming signal of up to 0.8°C below 200 m that fades with depth. Below 200 m, any increase in PC3 thus warms the entire water column until 2000 m. As for salinity, higher values of the third mode slightly lowers salinity (only 0.02 psu) until 300 m, and there are two inversions beneath the surface layer. Until 1200 m, an increase in PC3 clearly makes the intermediate waters saltier. A previous study utilizing the fPCA method with other data sources and shorter time frames showed slightly similar PC3 effects, even on a global scale (Pauthenet et al., 2019), and has linked the behaviour of the third mode to the depth of the pycnocline. However, the second inversion at 1200 m, below which salinity slightly decreases again, did not appear in another analysis using only data from 2007 (Pauthenet et al., 2017). The consequent effect on steric height is likely negligible, but it could be an indicator of slow oceanic changes (e.g. fresher AABW due to increased melting, if there would be an increase of

PC3 values over time). Here again, salinity is dominant (57%), even if considerably less than for PC2. The total influence on steric height variability can be expected to be relatively low, both as a a consequence of the small percentage share and the compensating behaviour of the water column.

In general, the effects of θ and S variations on sea level can be computed by using an approximation of the international EOS. Using a linearized approximation, the change in density relative to ϱ_0 can be explained by Equation 5.1:

$$\frac{\Delta\varrho}{\varrho_0} \simeq \alpha_0 \Delta\theta - \beta_0 \Delta S. \tag{5.1}$$

Here α_0 and β_0 describe the linear thermal expansion coefficient and linear haline expansion coefficient respectively. Using the definition of steric height anomalies (Equation 2.3), an approximate expression for the variations of steric height anomalies is obtained, with respect to PC_i values as a function of variations of temperature and salinity, so that

$$\frac{\Delta\eta}{\Delta PC_i} \simeq \alpha_0 \int -h \, \frac{\Delta\theta}{\Delta PC_i} dz - \beta_0 \int -h \, \frac{\Delta S}{\Delta PC_i} dz. \tag{5.2}$$

Using standard values (1 for α_0 and 8 for β_0; Madec et al., 2017) of a simplified EOS (S-EOS), the steric height change due to PC variations can be quantified. This can be exemplified by estimating the total anomaly of θ ($\bar{\theta}_i$) and S ($\bar{S}_i$) throughout the 2000 m water column when adding the eigenvalue of mode i to PCi with $i \, \epsilon \, 1, 2$ (see Table 5.1), so that

$$\frac{\Delta\eta}{\Delta\theta_{PC_i}} = \frac{1 * 10^{-4} * \bar{\theta}_i * h * 10^2}{10^2} \tag{5.3}$$

and

$$\frac{\Delta\eta}{\Delta S_{PC_i}} = -\frac{8 * 10^{-4} * \bar{S}_i * h * 10^2}{10^2} \tag{5.4}$$

with h as the height of the profile (2000 m) multiplied by 10^2 in order to be converted into hPa. The result is returned in meters.

The outputs of Equation 5.3 and 5.4 (converted to cm) reveal that a positive change of order 1 of the first mode increases steric height by 72 cm, while a positive change of order 1 of the second mode

decreases steric height by -30 cm (Table 5.1).

Effect	PC1	PC2
θ	**+80 cm** (Estimated anomaly: +4°C)	**-14 cm** (Estimated anomaly: -0.7°C)
S	**-8 cm** (Estimated anomaly: +0.05 psu)	**-16 cm** (Estimated anomaly: +0.1 psu)
Total	**+72 cm** (80 cm + (-8 cm))	**-30 cm** (-14 cm + (-16 cm))

TABLE (5.1) θ and S effect of PC1 and PC2 on steric height for one added eigenfunction, calculated with Equations 5.3 and 5.4.

It should be stressed that the results are based on estimations of mean θ and S changes observed over the water column. Still the result of the total steric height change serves as a generalised approximation of the potential effect the main modes create on steric sea levels.

5.2 Spatial Distribution of Modes

All monthly profiles of the domain have been projected on the above-defined basis to produce PC values for every grid point and month from 2008 to 2017. The resulting values can be analyzed in regards to their changing behaviour over time, as well as their regional distribution. To begin with, the mean PC values for the entire domain have been computed and plotted on a map to analyze the mean PC distribution of the main modes.
This section discusses the spatial distribution of the first three modes.

5.2.1 Mode 1

There is a clear large scale pattern with higher PC1 values in the northern part of the analyzed region and smaller PC1 values closer to the Antarctic continent (Figure 5.2). The higher PC1 values to the north can be explained by the temperature gradient of the surface waters. The subtropical surface waters are significantly warmer than the surface waters closer to the South Pole. Maps of the sea surface temperature (SST) gradient of the surface waters south of 30°S show a comparable spatial pattern. Roughly the same applies to salinity, with more saline surface waters in the subtropical regions and fresher waters to the south. Both of these observations are reflected in the effect of one added eigenfunction of θ and S respectively to the mean PC profile.

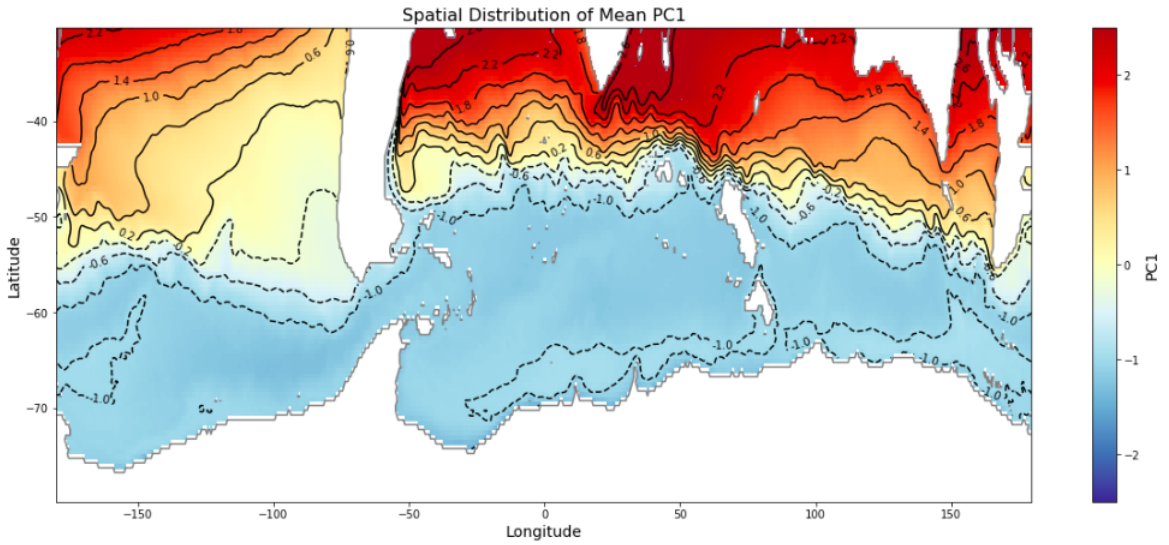

FIGURE (5.2) Spatial distribution of mean PC1 values from 2008 to 2017 plotted over the entire study domain. Contour Intervals = 0.4 with dashed lines indicating negative values.

It can be concluded that the θ and S gradient in the surface waters from 30°S to around 60°S dominate the overall variability of θ and S.

While PC1 alone explains a substantial part of the variance of temperature and salinity changes, it does not capture the stratification due to salinity and other more complex θ and S structures. South of the dashed -1.0 contour line between 50°S and 60°S, the PC1 value remains almost constant and thus does not capture prominent processes in the center and the southern area of the domain.

5.2.2 Mode 2

The distribution of mean PC2 values (Figure 5.3) does reveal gradients in the northern part as well as closer to the pole. Instead of a continuous decrease or increase of PC2 values from north to south, there are noticeably lower PC2 values in the circumpolar region of the ACC region (wide area around 50°S). With the effect of higher and lower values of the second mode on the vertical structure of θ and S profiles, it can be concluded that PC2 explains the lower salinity that is observable in the ACC area. It is also visible that, in contrast to longitudes in the Atlantic and Indian Ocean sectors, there is a noticeably wider area of lower PC2 values west of the South American continent. This could be attributed to the Humboldt current system transporting cold and fresh surface waters northward from Antarctica (Silva et al., 2009). The contour lines of PC2 towards the south as visible in Figure 5.3 further reveal the PF and the SACCF, which could not be identified from the mean PC1 distribution.

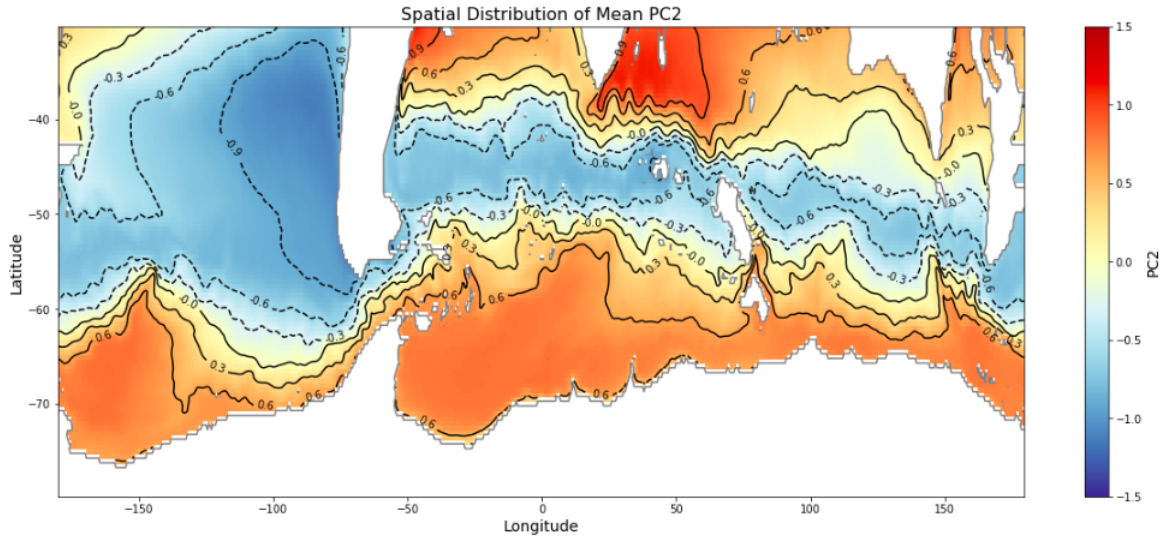

FIGURE (5.3) Spatial distribution of mean PC2 values from 2008 to 2017 plotted over the entire study domain. Contour Intervals = 0.3 with dashed lines indicating negative values.

5.2.3 Mode 3

The effect of positive and negative PC3 changes on the water column and its mean spatial distribution (Figure 5.4) is an interesting representation of more complex and local features that most of the higher modes cover (see A.1 and A.2 for the mean distribution of the fourth and fifth mode).

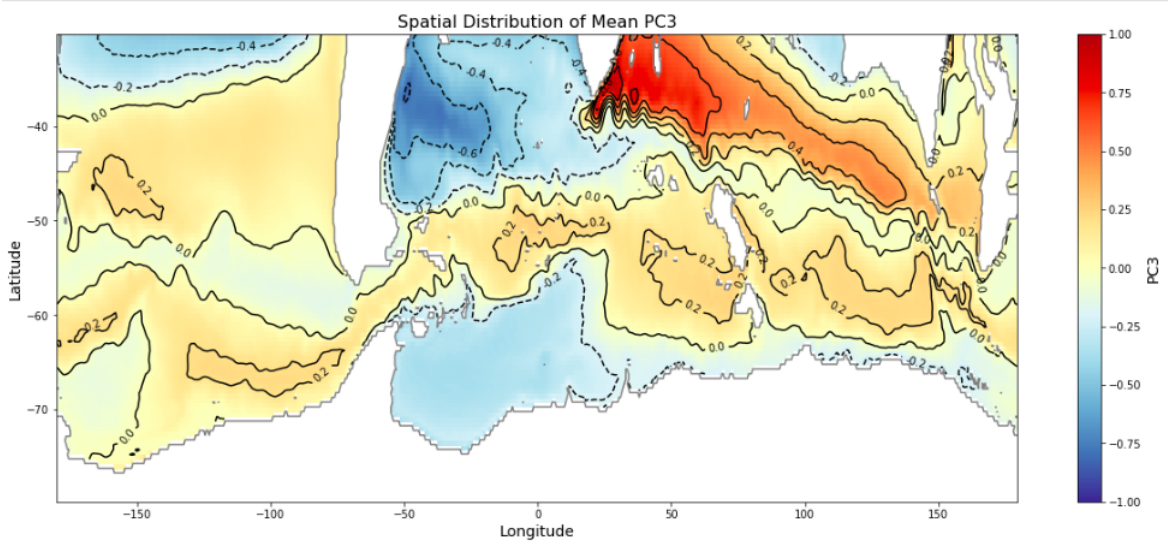

FIGURE (5.4) Spatial distribution of mean PC3 values from 2008 to 2017 plotted over the entire study domain. Contour Intervals = 0.2 with dashed lines indicating negative values.

In opposite to the first two modes, the third mode shows a pattern that is much less zonal. Instead of a north-south gradient, there are stronger signals in local areas such as the Weddell Sea (negative

values), the Falkland current (negative values) or the Agulhas current (positive values). Overall, there is a pattern of positive PC3 values in the Indian and a pattern of negative values in the Antarctic sector, with the exception of the ACC area (having a mean latitude at 55°S; Sun et al., 2002). The positive signal in the Indian basin could be attributed to the pycnocline being relatively shallow, especially compared to the Atlantic sector (Pauthenet et al., 2017; Nagura and McPhaden, 2018; Feucher et al., 2019).

Due to its non-zonal distribution and small potential influence on density changes, the third mode is not investigated as detailed as the first two modes hereafter.

5.3 PC1 and PC2 Distribution in the Space of Steric Height

The zero-centered steric height results vary from -96 cm to 160 cm (see table 5.1) and thus show a rough range of 1.5 m. Figure 5.5 shows all steric height data points as a function of PC1 and PC2.

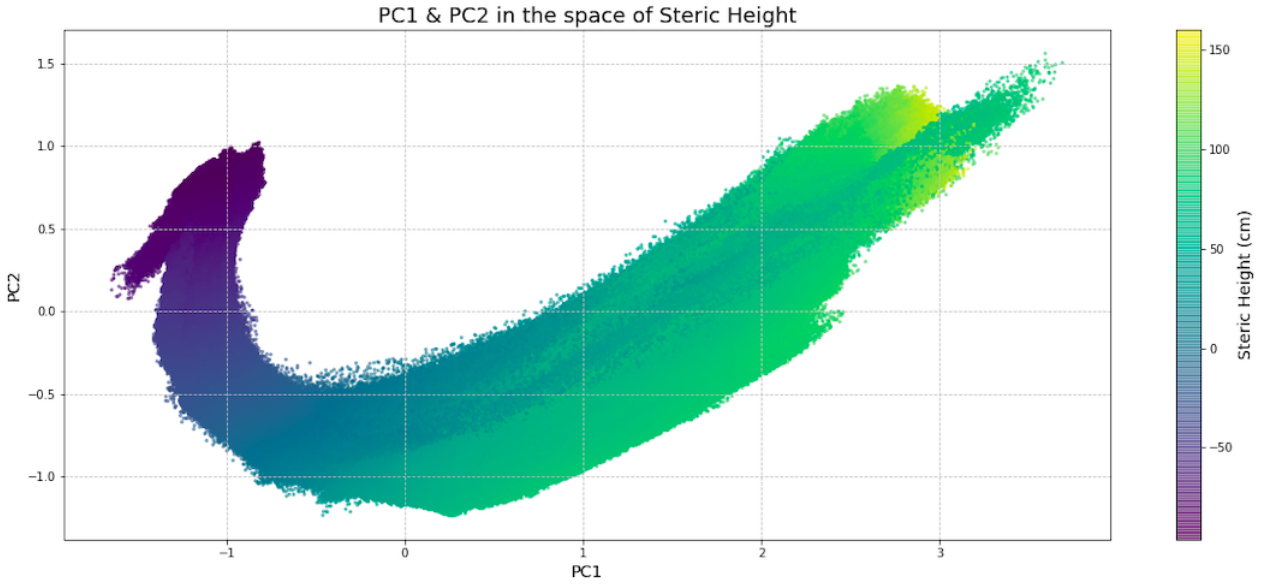

FIGURE (5.5) Steric height (in cm) of all grid points and months plotted as a function of the respective PC1 and PC2 values.

The scatterplot reveals that large steric height values are more likely to occur when both PC1 and PC2 are high. This means that the steric sea level of the study domain is highest when and where the waters are generally warmer, but also saltier. In theory, if steric height was analyzed as a function of all θ and S combinations, it would be highest where temperature is maximal and salinity is minimal.

As the warmest waters of this study domain are simultaneously very salty (namely the subtropical waters), the steric height in the present case is highest where both PC1 and PC2 values are high. This also means that the saltier waters that go along with higher PC2 values have a compensating effect on the density.
On the contrary, steric sea level is noticeably only low where PC1 is low. This shows that the second mode has a smaller weight in terms of its contribution to steric height variability. However it is noticeably controlling the density where PC1 is below 0. The dominant effect of salinity covered by the second mode enables higher PC2 values (and hence saltier waters) to increase the density where steric height is already low due to colder waters.

Mapping the time mean of steric height (Figure 5.6) confirms that the temperature gradient from north to south as captured in the PC1 distribution is portrayed in a continuous decline of steric sea level.

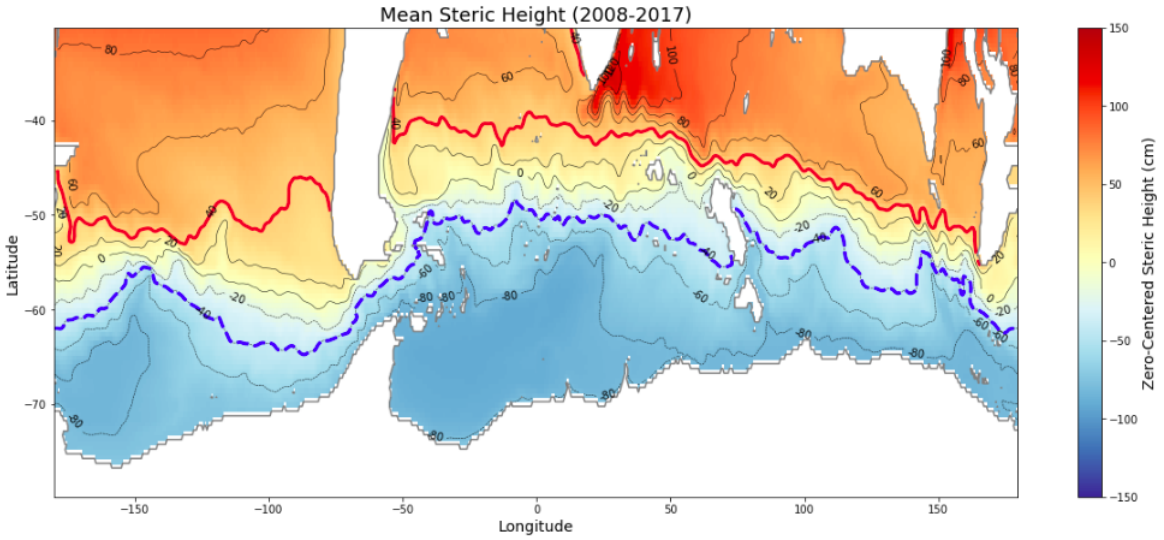

FIGURE (5.6) Map of mean steric height in cm (2008 to 2017). The red contour line indicates the southern limit of the subtropical sector (40 cm) and the blue dashed contour line indicates the northern limit of the Antarctic sector (-40 cm) chosen for this study.

This implies that the first mode is responsible for the steric height decline until roughly 50°S. As the PC1 values farther south have an almost constant value of -1, it can be concluded that the subsequent north-south decline of PC2 in the ACC and southernmost waters is a consequence of the salinity gradient captured by the second mode (Figure 5.3). There is a clear gradient in PC2 from south of 50°S until 70°S indicating a change from fresher to saltier waters, that explains the increase in density towards Antarctica (Figure 5.6) despite the lack of a mean PC1 gradient in this region.

The increasing values of PC2 are also portraying the colder temperatures at the surface towards the Antarctic coast, as captured by the less influential effect of temperature on PC2.

In order to regionally characterize the distribution of the steric height data points in the space of PC1 and PC2 as discussed above, the data was separated into sectors based on their steric height ranges (Figure 5.6). The superimposed red and blue contour lines organize the study domain into three sectors: The subtropical sector (all steric height values above 40 cm), the Antarctic sector (all steric height values below -40 cm) and the subantarctic sector (all steric height values in between). Instead of defining circumpolar regions based on fixed latitudes, a division based on steric height ranges provides a more natural and realistic separation of the different water masses. Based on the three different regions, Figure 5.7 shows a colour-plot version of Figure 5.5 describing where the defined data points are located. Here the same data points of PC1 are plotted against PC2 and marked with the colour representing the regions as defined ad-hoc. The plot shows that there is a clear space for all PC1 and PC2 combinations with only minor regions of overlaps.

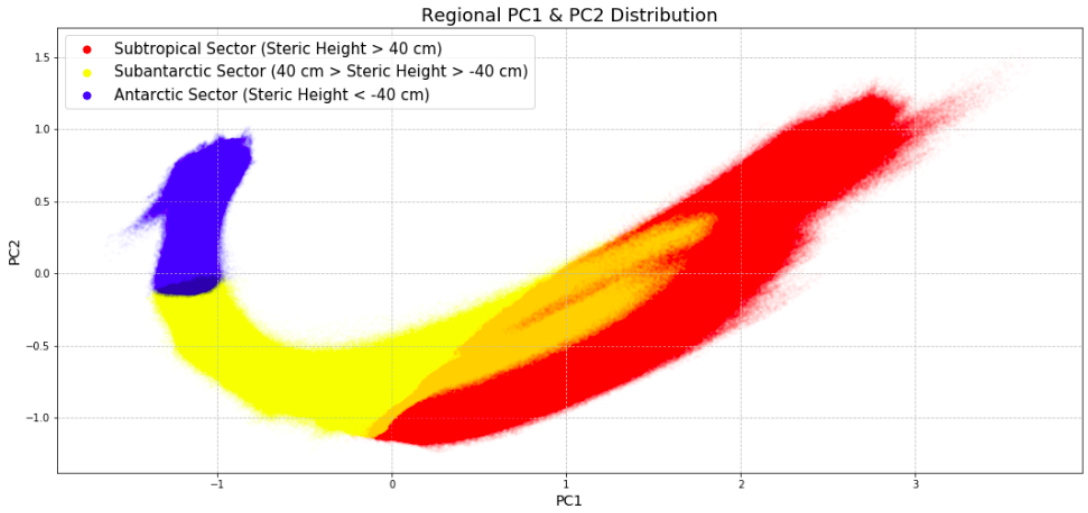

FIGURE (5.7) Monthly (2008 to 2017) PC1 values plotted against PC2 values of all grid points characterized by colour: Red indicating the subtropical sector, yellow indicating the subantarctic sector and blue indicating the Antarctic sector. Orange and dark blue colours indicate overlapping data points.

As suggested before, the waters of the subtropical sector have a high range of both PC1 and PC2 values. They also show the greatest distribution in the PC1 and PC2 space, which is the consequence of a rapid decrease in θ and an increase in S from north to south. PC2 increases almost linearly with warmer waters (as captured by PC1), which again demonstrates the compensating effect of salinity

on steric height.
The subantarctic sector is characterised by colder and fresher waters compared to the subtropical sector. The curved shape of the steric height cloud of this sector in the PC1 and PC2 space is most likely a sign of the transition from PC1 dominating the steric height to PC2 dominating the steric height. Waters in the subantarctic region range from colder and saltier closer to the south over fresher waters to warmer, and again saltier towards the subtropical domain. In the colder regions where PC1 is around -1, PC2 varies slightly more than in warmer waters.
The steric height data of the Antarctic sector has the densest distribution amongst possible PC1 and PC2 combinations. The blue patch of PC1 values ranging from -1.5 to 1.2 and mostly positive PC2 values (-0.2 to 1) reveal the region of the coldest and freshest waters of the Southern Ocean. Although these fresher waters in the Antarctic sector are less dense than the saltier waters in the subtropical sector, the drop in temperature close to Antarctica drives lower steric sea levels.

It can be concluded that temperature controls the steric height variability in the subtropical part of the study domain, while salinity becomes increasingly more important in the subantarctic region and clearly dominates southernmost steric height changes.

5.4 Steric Height as a Function of PCs

A reasonably adequate prediction of steric height can already be achieved by using the first mode only (Table 5.2). Naturally, the additional information contained in the modes result in changes in explained variance that are strongly related to the covered variance of the θ and S changes discussed above. PC1 explains 80.5% of the steric height variance, meaning most of the observed variability is linked to temperature changes especially in the first 1000 m below sea level, along with inversions of the haline structure (Figure 5.1). The second mode adds 17.28% and therefore almost the entire remaining variance to the predictive model. Especially after introducing the third mode to the model, the added information of higher modes is close to zero, although they can have significant meaning for local variations of θ S (Pauthenet et al., 2017).

In order to directly compare the PC values to steric height, they can be multiplied by their respective MLR coefficient. Table 5.2 shows how the coefficients of the modes change each time one additional mode is introduced to the model. It is apparent that especially after each truncation, the total change of covered variance becomes almost negligible. Included is also the root mean square error (RMSE)

to show how far spread out the residuals of each model and order are, as well as the R-squared R^2 to show how close the fit is when measured relatively.

Order	a_1	a_2	a_3	a_4	a_5	*RMSE*	R^2
1^{st}	45.403	-	-	-	-	747.72	0.8049
2^{nd}	45.5019	-41.712	-	-	-	85.54	0.9777
3^{rd}	45.514	-41.752	33.524	-	-	9.20	0.9976
4^{th}	45.512	-41.755	33.5	-4.932	-	8.46	0.9978
5^{th}	**45.511**	**-41.753**	**33.485**	**-4.932**	**-2.189**	8.40	0.9978

TABLE (5.2) PC coefficients for all MLR models of order 1 to 5, and their performance results presented as RMSE (in cm) and R^2 values. Bold coefficients represent those used for the following regression analyses.

For the reconstructions of steric height as a function of one or more modes, the PC values have been multiplied by their coefficients corresponding to steric height as a function of all five modes. Therefore steric height is reconstructed as a linear sum of the variations

$$\eta_{\mathrm{i}} = 45.511 * PC1_{\mathrm{i}} - 41.753 * PC2_{\mathrm{i}} + 33.485 * PC3_{\mathrm{i}} - 4.932 * PC4_{\mathrm{i}} - 2.189 * PC5_{\mathrm{i}}, \tag{5.5}$$

where i represents one of 6,090,240 data points.

5.5 Temporal Variability of Steric Height and the Thermohaline Structure

This section represents the core of the analysis, with the focus lying on temporal variability. It is organized as follows: First the time series of the entire domain is investigated to demonstrate the average development of the modes and the steric height. This is followed by a zonal analysis based on linear trend slopes of all latitudes from 30°S to 70°S. In order to then discuss the linearity of these trends in a feasible way, the time series of the predefined sectors (Subtropical, Subantarctic, and Antarctic sector) are being analyzed.

5.5.1 Spatial Steric Height and Mean PCs over Time

The mean of the entire study domain of the first two modes and the steric height have been computed for all months. Steric height and PC seasonality are briefly addressed because they contain information about how steric height is affected by seasonal changes of the modes and also serve as an indicative classification for the magnitude of non-seasonal changes. It is important to mention that computing the spatial mean omits the differences of the distinct water masses. Differences in the seasonal and long-term behaviours of the modes and the steric height can lead to compensation, which is discussed in the following sections.

Decomposing PC1 and PC2 into trend and seasonality does reveal two important findings: The anticorrelation of the seasonal PC1 and PC2 changes and the slight upward trend (1.86 * 10^{-3}/yr for PC1 and 1.00 * 10^{-3}/yr for PC2) of both time series (Figure 5.8).

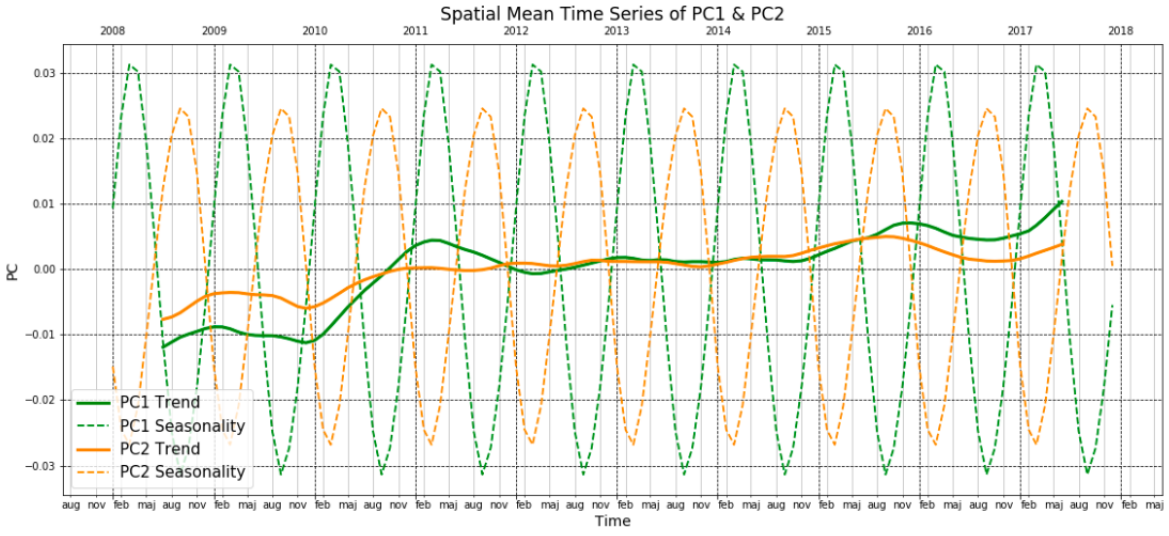

FIGURE (5.8) Trend (solid lines) and seasonality (dashed lines) component of spatial mean PC1 and PC2 values from 2008 to 2017. PC1 trend slope = 1.86 * 10^{-3}/yr with a R^2 = 0.75 (p-value= 0.000); PC2 trend slope = 1.00 * 10^{-3}/yr with a R^2 = 0.73 (p-value= 0.000).

The negative intra-annual correlation is a consequence of the different responses of the first and the second mode on the changing seasons. In the first half of year, PC1 values are positive due to higher SST of the subtropical water masses in austral summer and autumn. PC1 reaches its maximum in March and decreases thereafter, until reaching its minimum in September. PC2 values are negative from January to June and positive the other half of the year. In the high-latitude waters, this can be related to an increase in salinity during winter and spring when sea ice is forming. The formation

leads to a rejection of salt from the ice (brine rejection), that slowly sinks to the waters underneath. Meanwhile, the subtropical waters are colder during autumn, especially at the surface (referencing Figure 5.1, upper right panel).

Compared to the seasonal fluctuations, the variations and the absolute rise of the mean trend components of PC1 and PC2 are small. Still both time series have a significant linear trend that explains most of the variance (R^2 of PC1 = 0.73; R^2 of PC2 = 0.75). Using the linear decadal trend along with the estimated mean increase in θ per added eigenfunction of PC1 (+4 °C), there is a mean temperature rise of 1.86 * 10^{-2}/yr = 0.074 °C over the Southern Ocean. The linear S trend and estimated mean increase in S per added eigenfunction of PC2 (+0.1 psu) portray a total increase of 1.00 * 10^{-2} * 0.1 = 1 * 10^{-3} psu from 2008 to 2017.
Both trend components follow similar developments over the years, starting with constant negative values, followed by an increase in 2010 and a noticeable stagnation from 2012 to 2015. Although they both have lower values in 2016, they show an increasing tendency from then on.

In order to investigate the effect of these seasonal and trend-related changes on steric height, the same decomposition was performed on the spatial mean steric height data (Figure 5.9).

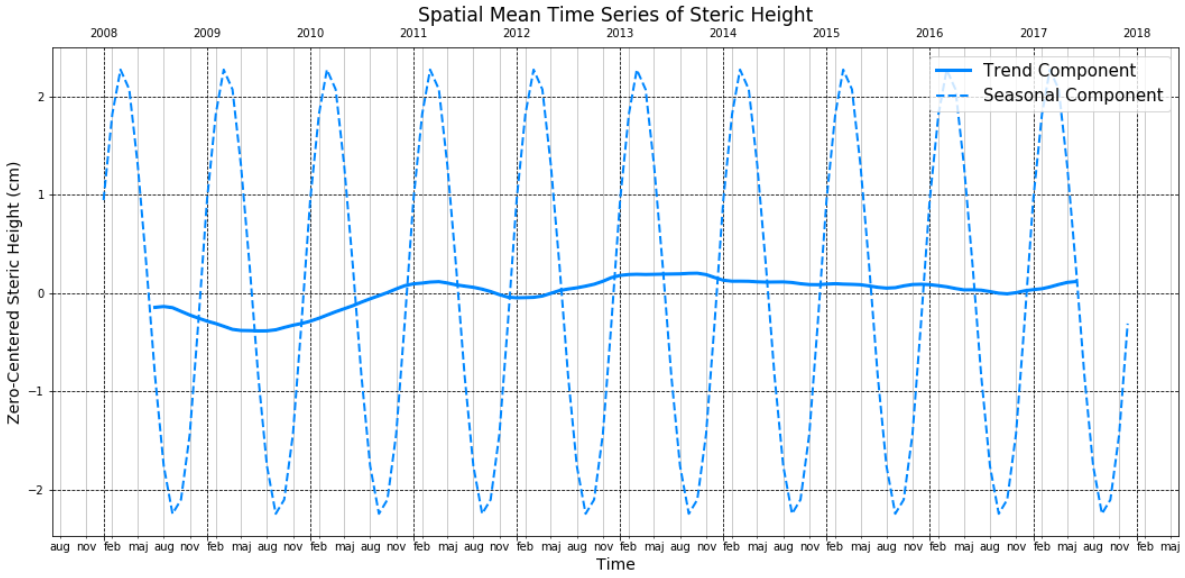

FIGURE (5.9) Trend (solid lines) and seasonality (dashed lines) component of the spatial mean steric height values as a function of time. Trend slope = 0.416 mm/yr with a R^2 = 0.44 (p-value= 0.000).

As positive values of the first mode are related to higher steric sea levels, while positive PC2 values

lower the steric sea level, the mean steric height of the Southern Ocean shows a strong seasonal signal with higher values during summer and autumn, and lower levels in the winter and spring months. The resulting steric component of sea level in the Southern Ocean is therefore 4.5 cm higher in March than it is in August.

The fluctuating trend line of steric height is not linear and has a positive mean linear trend of 0.42 mm per year. This linear trend is significant and moderately accurate (R^2 = 0.44), but less linear then that of the modes. Here the positive trend of PC2 is partly compensating the thermal expansion generated by the positive PC1 trend.
This linear trend in steric height could be approximated by combining the effect of one added PC eigenfunction on steric height with the MLR coefficients. Multiplying the linear PC trend slopes by their coefficients and their approximate effect on steric height (Table 5.1) provides an estimated trend of 1.86 * 10^{-3} * 0.45511 * 72 + 1.00 * 10^{-3} * (-0.41753) * 30 = 0.0609 - 0.0125 = 0.048 cm/yr = 0.48 mm/yr (here the MLR coefficients have been multiplied by 10^{-2}, since the conversion to cm is already met) that is very close to the actual trend. The small difference (0.06 mm/yr) is mostly due to uncertainties of the steric height approximation per added eigenfunction, as well as a result of only using the first two modes. The usage of the S-EOS equation combined with a regression model allows to quantify the respective contributions of the modes, and, if needed, the respective θ and S contribution (Equations 5.3 and 5.4). The global mean trend of steric height over the investigated decade due to the PC1 and PC2 can herewith be quantified as ∼0.60 cm and ∼-0.13 cm respectively. To understand the compensation due to thermohaline variations and regional differences that produce the small trend in steric height, a more detailed and regional approach is needed.

5.5.2 Regional Analysis based on Zonal Linear Trends

This section demonstrates that the global domain mean trend slopes of steric height and the modes are not valid representations for all latitudes. Instead, there are large differences between zonal regions that are balancing out positive and negative trends. Here the focus lies exclusively on linear trend slope values, hence degree fluctuations (i.e. non-linear changes of the trends) are not considered yet (see section 5.5.3).

In Figure 5.10, grid points with a positive (negative) linear trend are presented in red (blue). The map reveals that in the South Atlantic Ocean the linear steric height trend decreases from north to south. In the Indian Ocean this gradient is also present, but less clear, with deviations south of Australia and near the Agulhas current south-east of Africa, where steric height has decreased over time. From 40°S

poleward, the overall trend distribution is very comparable to that of the Atlantic and West Pacific sector. Only in the East Pacific domain, a dominant decrease or increase in steric height along the latitudes is not present. Instead, steric height has fallen in the higher and lower latitudes of the study domain and risen in between.

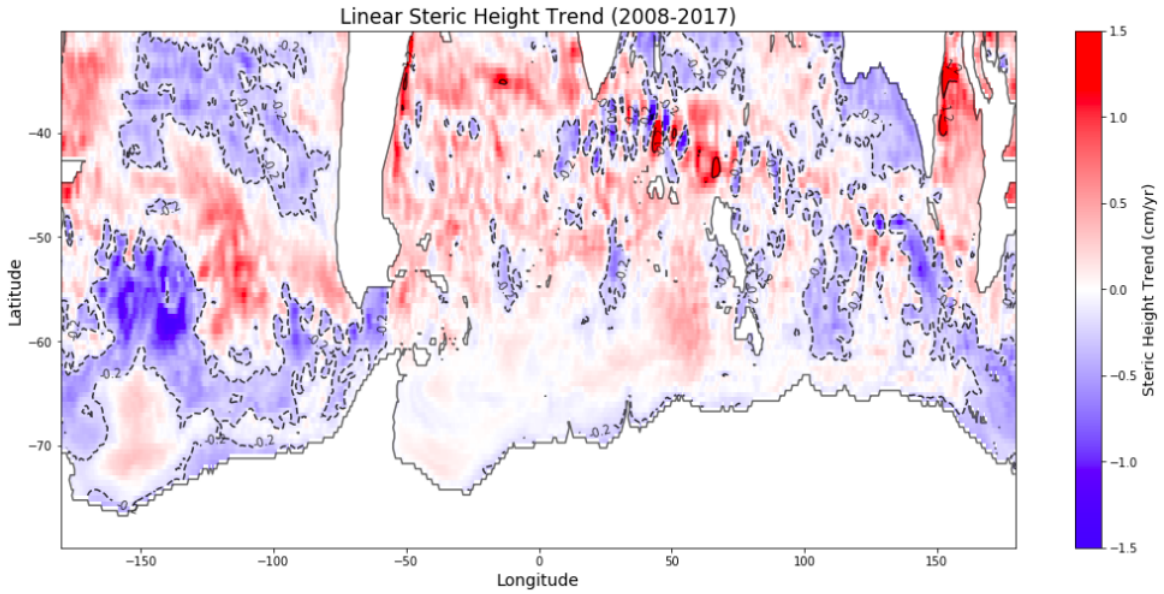

FIGURE (5.10) Map of the linear trends of steric height in cm/yr (from 2008 to 2017) with red colours representing positive and blue colours representing negative linear trend slopes.

Comparing the spatial trend distribution of steric height with that of the first two modes (A.4) reveals the causes for those divergent regional trends. In the subtropical sector of the East Pacific, where steric height variations are mainly dependent on temperature changes, steric height has dropped (except for waters close to the South American coastline). The Amundsen Sea has been subject to decreasing temperatures as well, along with an increase in salinity. This explains the special case of the East Pacific steric height trend distribution (Figure 5.10), even if underlying causes for θ and S and changes remain undefined at this point. In the West Pacific sector, surface waters have become significantly warmer, and intermediate waters have become saltier at nearly all latitudes. In the Indian, the Atlantic and the Central Pacific Ocean domain, the linear trend is dominantly positive in the subtropical and Antarctic sector, and negative in between.

While it is thus reasonable to discuss the differences from a zonal perspective (as followed), a complementary analysis and discussion of differences between ocean basins could explain deviating behaviours.

In order to discuss the temporal θ, S and steric height relation in an ordered structure, this section presents and discusses linear trend slopes of steric height as zonal averages (Figure 5.11).

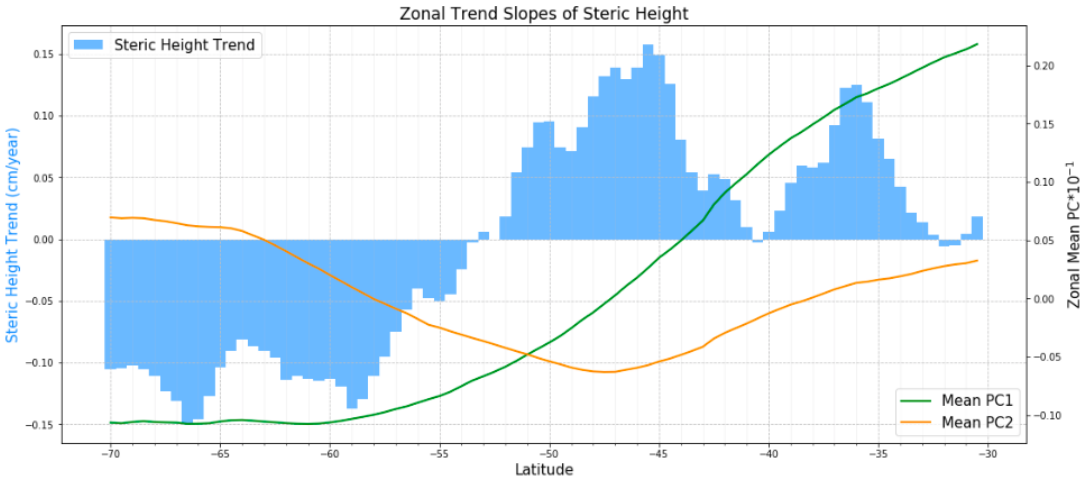

FIGURE (5.11) Linear trend slopes of steric height at every 0.5^{th} latitude from 30°S to 70°S. Mean values of PC1*10^{-1} (green line) and PC2*10^{-1} (orange line) plotted on top. The decimal place is of no importance here as the PCs have no unit.

The trend slopes for the zonal analysis have only been computed for all latitudes north of 70°S, strictly speaking for every 0.5^{th} latitude. Oceanic areas south of 70°S are restricted to complex systems that are more separated from each other, such as the Weddell Sea and the Ross Gyre. Moreover, the data of the southernmost waters close to the Antarctic coast are less reliable as the observations on which the GLORYS model is based on are especially sparse (Riser et al., 2016; Roemmich et al., 2019; Storto et al., 2019a).

The green and orange graphs represent the mean mode values (not the trend slopes) of PC1 and PC2 multiplied by 10^{-1}. Here the modes have not yet been multiplied by their regression coefficients in order to focus on their information in terms of the θ and S structure. The direct effect that the mean of PC1 and PC2 have on steric height from a zonal perspective is illustrated in A.3.
The mean values of both modes plotted on top provide a plausible explanation for why the steric height trends are changing from positive to negative between 50°S and 55°S. The PC graphs show that this is also the zone where the mean PC1 and PC2 values cross each other, meaning that waters south of this zone are dominated by salinity changes, while being dominated by temperature north of it. It is in this zone where the mean position of the PF is located (Freeman et al., 2016), representing the southernmost front that the mean PC1 map can identify. The Polar Frontal Zone (PFZ, between the SAF and the PF) has previously been identified as the zone where the stratification of the ocean

is neither dominated by temperature, nor by salinity (Pollard et al., 2002; Pauthenet et al., 2017). The steric sea level south of the PF is no longer exposed to the rising temperatures represented by the positive trend of the first mode, and is instead falling as a consequence of the positive PC2 trend indicating more saline waters. This could be regarded as a plausible explanation as to why there is no noticeable trend in the PFZ.

The second trend close to zero, this time represented as a minimum of a through at 40°S, can also be related to the position of a major front. The location corresponds to the STF, that separates the significantly warmer subtropical waters from colder waters to the south.

To fully understand the distinct patterns of the zonal steric height trends, the same trend slope calculations were performed on the first two modes (Figure 5.12).

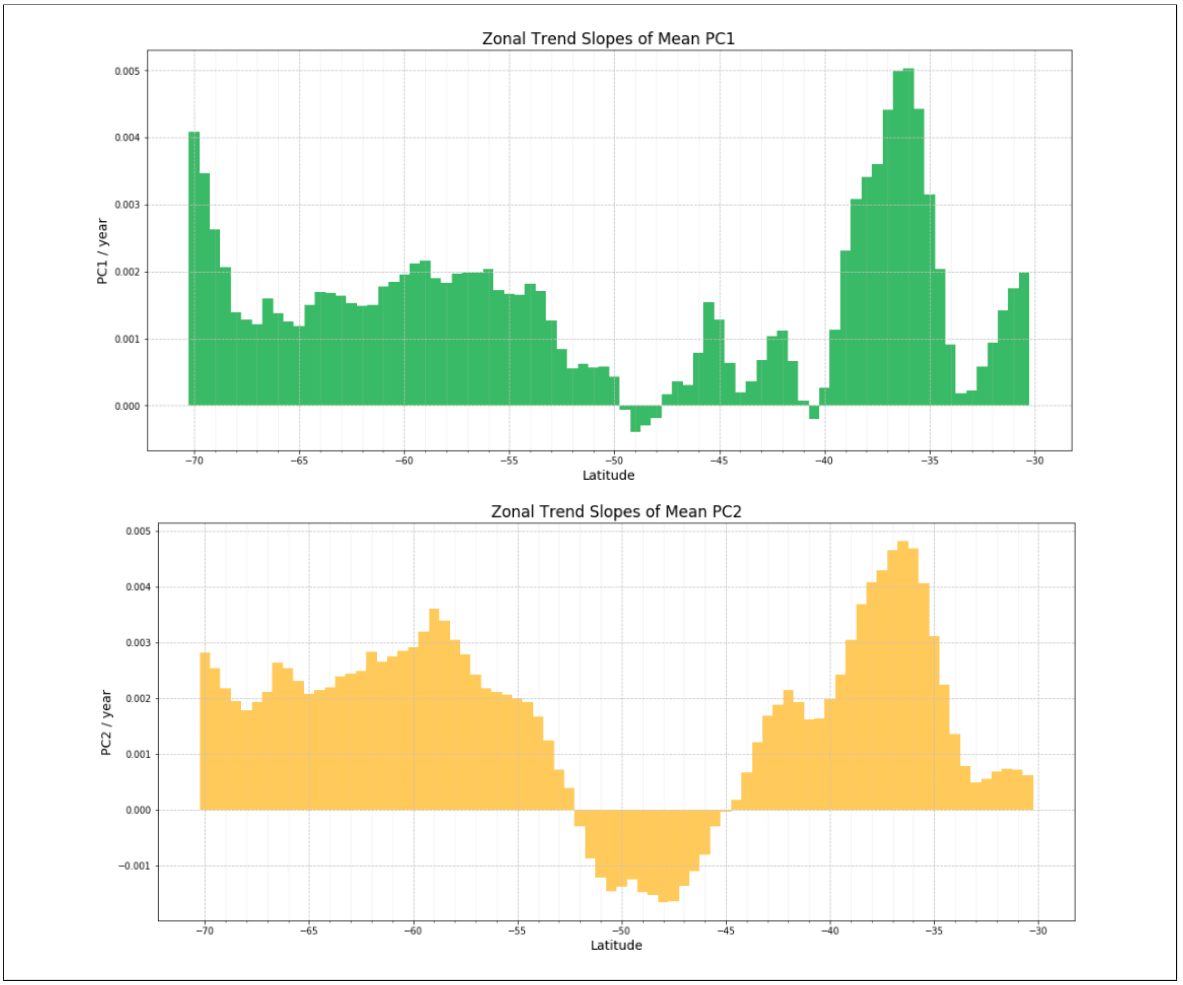

FIGURE (5.12) Linear zonal trend slopes for every 0.5^{th} latitude from 30°S to 70°S. Upper panel (green bars): PC1; Lower panel (yellow bars): PC2.

The zonal trend slope results of the first two modes confirm that the positive global domain PC1 and PC2 trends are present at almost all latitudes. This is an important indication that the increase in salinity, represented by positive PC2 trends, has a compensating effect on the increase in temperature, represented by positive PC1 trends.

The first mode only has a slightly negative or close-to-zero trend in the subantarctic zone (SAZ, between the SAF and the STF). This region is also related to a freshening of intermediate waters, as revealed by the negative PC2 trends from 45°S to 52°S. Remarkably, earlier studies investigating warming trends since the 1950's have ascribed this zonal sector (40°S to 50°S) to the one where the Southern Ocean warms the most (Gille, 2008; Stocker et al., 2013; Armour et al., 2016). The relatively low PC1 trends in these zones thus either tend to originate from the salinity information of first mode (freshening of intermediate waters), or indicate a change of the θ trend in recent years. Indeed it is plausible to suggest that the long-time warming of the SAZ has damped additional surface heat uptake and has consequently led to a much smaller or even negative trend since then. Even south of the ACC, from 52°S towards the Antarctic coast, PC1 shows constant positive linear trends that even increase closer to 70°S. This indicates a significant warming of the upper water column along with an increase in sea surface salinity (SSS). Chapter 5.5.3 shows that the positive decadal trend shown here arises exclusively from all years from 2014 onwards, which (if this trend continues) could hint towards the beginning of the delayed warming of waters far to the south.

At all latitudes in the subtropical domain, where both PC1 and PC2 show strong positive trends, the salinity-driven compensating factor of PC2 is not sufficient to offset the positive steric height trend induced by the warming of waters. This condition differs from areas south of the PF, where salinity dominates the stratification: Although the trends of the first mode are clearly positive, the trend of the second mode seems to be the critical cause for the negative steric height trend south of 53°S. The effect that PC2 adds to the effect that PC1 alone would induce on the steric height trends is shown in Figure 5.13. For the creation of this plot the respective impacts of the modes have been visualized by using the MLR model to predict the zonal steric height trends. Here the trends of the mean zonal PC values have been multiplied by the model coefficients in order to directly predict the steric height trend slopes. The green dashed line indicates the steric height predicted by PC1 only and therefore depicts the exact trend values of PC1 itself. Adding the second mode to the prediction of the trends (orange dashed line) is crucial. Depending on the region, the higher modes act to further raise or lower steric sea levels and allow for closer approximations of the actual trends.

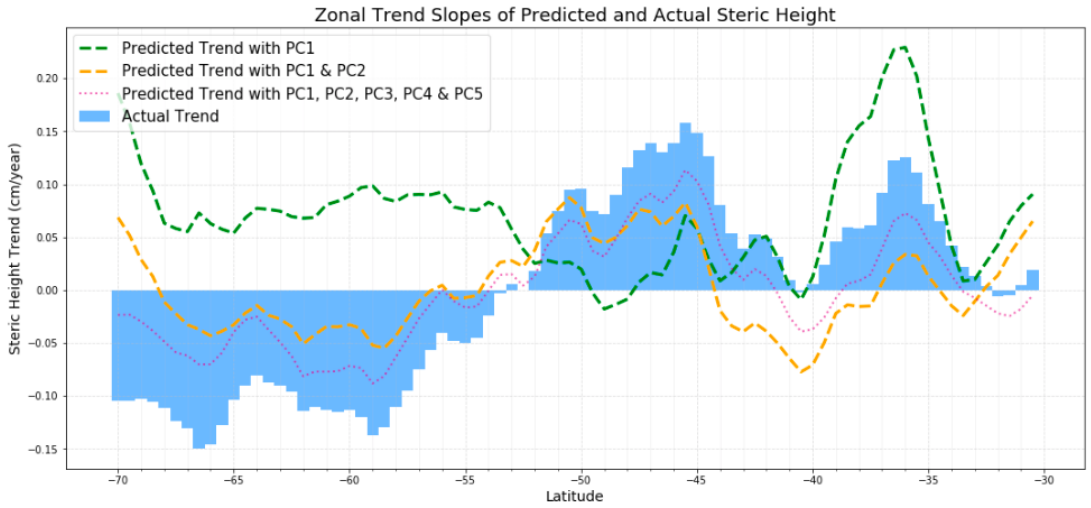

FIGURE (5.13) Linear trend slopes of steric height values for every 0.5^{th} latitude from 30°S to 70°S. Predicted steric height results from the MLR with PC1 (dashed green line), PC1 and PC2 (dashed orange line) and all five modes (thinly dotted purple line).

It is also remarkable that, at higher latitudes, where the first mode has a much smaller effect on the stratification, there is a relatively constant positive trend with a rising tendency towards the Antarctic coast. The winter sea ice partly extends north until the PF, meaning that a relatively large percentage of the warming trend south of the PF affects seasonally sea-ice covered regions. Despite this, research has shown that in opposition to the Arctic, the sea ice in the Southern Hemisphere has been expanding over the last decades until recently. This trend has lasted until 2015 and has been related to katabatic winds (Nghiem et al., 2016; National Academic of Sciences, 2017). Since then it has reversed, with a drapid decrease of Southern Ocean sea ice extent from 2015 to 2017. Although the extent is now slightly recovering again, it remains significantly lower compared to the 1981–2010 average (Scott, 2019).

The compensation of increasing salinity does not only derive from the second mode, but is also already included in the salinity contribution of the first mode. Higher values of both modes indicate saltier surface waters (PC1) in addition to saltier intermediate waters (PC2).

The general north-south trend gradient in steric height is also interesting in consideration of the already prominent zonal decrease of mean steric height values from north to south (Figure 5.6). The respective trend gradients steepen the slope of higher steric sea levels to the north and lower levels to the south, which thereupon results in stronger pressure gradients. Such modifications are typically reflected in an intensification of present currents. The ACC is a dominantly wind-driven current that was indeed subject to increased transport volume within the last decades, controlled by the Southern

Annular Mode (SAM). In the Southern Hemisphere, stronger winds blowing from east to west increase the Ekman transport anomaly to the left of the wind direction due to the Coriolis force. As the ACC intensification has so far been mainly attributed to stronger westerly winds in recent years (Farneti et al., 2015; Liau et al., 2017), it can be expected that the apparent steric effect contributes to the enhanced ACC transport.

5.5.3 Non-linear Trend Variations: Subtropical, Subantarctic and Antarctic Sector

One of the main results so far is that PC1 and PC2 are rising at almost all latitudinal ranges, while steric height rises in the subtropical, and falls in the Antarctic sector, as a consequence of PC2 dominating stratification of higher latitude waters. It is then of interest to investigate whether the trend slopes arise from nearly linear trend courses or inconsistent patterns with abrupt changes.
The three sectors defined in chapter 5.3 offer a reasonable organisation of the zonal differences in steric height. Here the subtropical sector captures the rising water masses, the Antarctic sector captures the falling water masses (here again until 70°S), and the subtropical sector captures the transition zone. The seasonally removed time series of these three domains (Figure 5.14) provide indications on whether the courses of the respective trend component prefigure a continuing increase/decrease from now on.

The positive steric height trend in the subtropical sector is primarily a result of a non-consistent increase until 2014. From then on, the monthly data outline a consistent decline in steric sea level until the beginning of 2017, which reduces the linear trend to 0.9 mm/yr and the explained variance to $R^2 = 0.23$. With a time period of 10 years, this signifies a trend of almost 1 cm per decade.
In the subantarctic sector the linear trend is not significant (p-value: 0.17). There are two noticeable minima at the end of 2009 and 2013. If the following linear upward trend was to continue, this could indicate a southward shift of the ACC, which would explain why steric height rises most at the northern boundary of the ACC (Figure 5.13).
The non-seasonal course of steric height in the Antarctic sector shows greater deviations from its linear trend since 2013. However the negative trend in steric height remains significant and predicts an annual fall in steric height of -0.2 mm/yr with an R^2 value of 0.31.
The positive (negative) linear trend in the subtropical (Antarctic) sector and the non-linear trend in the subantarctic sector can be explained by the respective non-seasonal trend courses of the first two modes (Figure 5.15). Here, the original PC values are shown instead of their exclusive direct effect η_{PC1} and η_{PC2} on steric height. Depicting the original mode values facilitates to explain variations

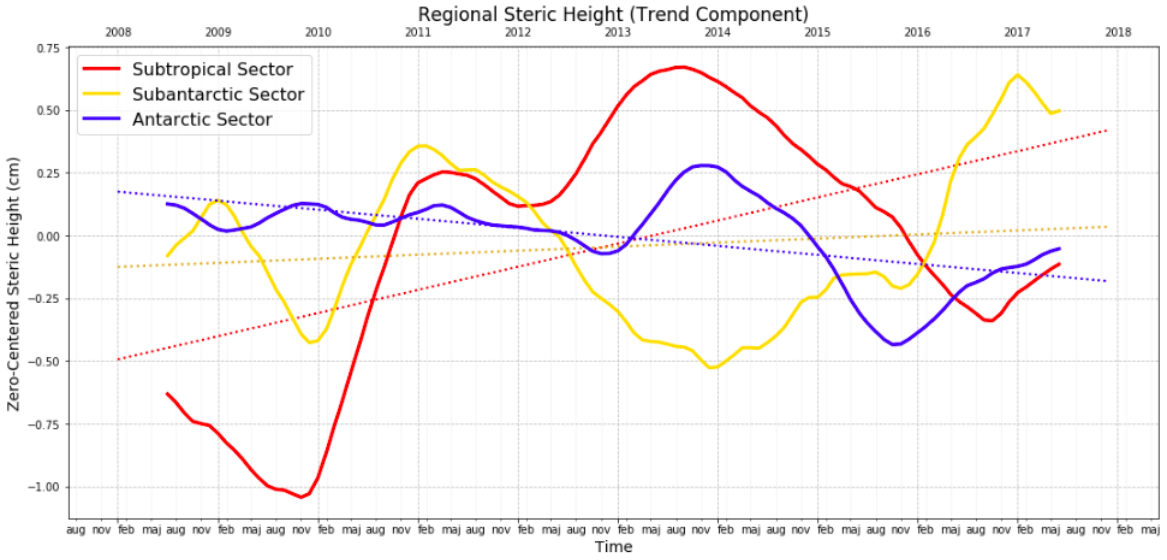

FIGURE (5.14) Seasonally removed time series of steric height (cm) in the subtropical (red solid line), the subantarctic (yellow solid line), and the Antarctic (blue solid line) sector from 2008 to 2017. Dotted lines indicate linear trend slopes of the respective sectors (Subtropical sector: $R^2 = 0.23$; Subantarctic sector: Trend not significant (p-value=0.17); Antarctic sector: $R^2 = 0.31$)

of the thermohaline structure and to understand the response of steric height. The respective time series of η_{PC1} and η_{PC2} are featured in A.6 and accurately display the PC effects on steric height as discussed below.

FIGURE (5.15) Seasonally removed monthly time series of PC1 (green line), PC2 (orange line) and steric height (blue line) in the subtropical (upper panel), the subantarctic (middle panel) and the Antarctic (lower panel) sector from 2008 to 2017. Monthly values of mode 1 and 2 have been multiplied by 10^2 for better comparison. Steric height data in cm (see changes in scales).

There is a drastic increase of the first mode in 2010 in the subtropical sector. Almost all of the total increase in temperature over the investigated decade has happened during one single year. The thermal expansion results in a total steric height rise of 1.25 cm in 2010, which is only slightly compensated by an increase in salinity (simultaneous rise of PC2). The fall of PC1 from then on is the dominant reason for the decline of steric height after 2014, as PC2 almost remains constant from 2014 until 2016. It does however not seem as if the warming in the subtropical domain has stopped, as the PC1 course shows a positive trend from 2016. The positive effect on steric height in this case is only slightly visible, as a result of a sharp increase in PC2 from 2016 to 2017 that compensates the warming-induced SLR. The reason for why PC2 rises and falls almost simultaneously to PC1 lies in the strong correlation (Pearsons r = 0.93) of the first two modes that is also present in the Antarctic sector. It is not clear why there is a significant increase of salinity in intermediate waters in 2016. Nevertheless, the salinity-driven contribution of the second mode to the steric height in subtropical waters is relatively small. It can be concluded that the positive decadal steric height trend of the subtropical domain is primarily a result of a strong warming event in 2010. Further there is no recognizable drop in temperature afterwards, which could indicate heat storage.

The almost-zero trend in the subantarctic region is a result of both PC1 and PC2 following an inconsistent, overall negative trend, with the exception of PC1 rising from 2016. This warming trend is related to the course of PC1 in the sutropical domain and could be an indication of a poleward shift of the ACC, resulting in greater heat storage at slightly higher latitudes.
In contrast to the subtropical sector, neither salinity nor temperature explicitly dominates the stratification of the water column. Due to the overall dominant effect of the first mode, the course of steric height is still mainly influenced by temperature (PC1) changes, and additionally modified by salinity variations (PC2). However the added information contained in PC2 explains most of the remaining variance (see steric height reconstruction in Figure A.6). While there is no distinct pattern of temperature changes in the subantarctic sector, the decrease in salinity is more distinct and translates into an overall freshening of the subantarctic waters surrounding most of the ACC. Here, PC1 and PC2 are not correlated to each other (Pearsons r = 0).

Compared to the subtropical and the subantarctic sector, the variations of both steric height and the modes in the Antarctic domain are relatively small (see different scaling of y-axes). Before 2014, there are only slight variations in PC1 and PC2, and consequently steric height. Yet it is already apparent that the non-seasonal trend steric height tends to rather follow the saline mode (noticeable in the asynchronous curve behaviour of PC2 and steric height): Unlike the domains farther north,

steric height is not primarily defined by temperature-induced changes.
PC1 and PC2 are again positively correlated, even if less significant than in the subtropical domain (Pearsons r = 0.61). This positive correlation becomes particularly obvious in the simultaneous rise from 2014 - 2016. Herein further lies the justification for the overall fall of steric sea level south of the ACC. Despite the clear warming trend during this period, there is a significant drop in steric height (0.7 cm) from 2014 to 2016. The strong increase in salinity until 2016 thus almost exclusively explains the general negative steric height trend in the Antarctic sector. Although PC2 drops after reaching its maximum in late 2014, it remains higher than the years before 2015 and therefore potentially keeps the steric height of the higher latitudes fairly low in the following years.
Despite the fact that temperature does not influence steric height variability as great as in the two sectors farther north, it is remarking that the positive trend at the higher latitudes (Figure 5.11, upper panel) almost solely arises from 2014 onward. In contrast to the increasing trend in salinity, it appears that the warming trend is more persistent. It is also very likely that in this case, the increase in salinity when adding the eigenfunction to the first mode is greatly supporting this positive PC1 trend in the south. A possible explanation combining both the θ and the S effect is the wind-induced northward transport of water that is slowly being substituted by the saltier and warmer NADW. This assumption can be backed up by recent studies showing that the hydrological effect of increased freshwater has freshened the southernmost waters, whereas wind-induced Ekman pumping has brought up warm and saline subsurface waters (Haid et al., 2016; Shi et al., 2020; Clément et al., 2020). Shi et al. (2020) have further suggested that the wind effect caused by stronger westerlies compensates the surface freshening and that overall, the effects of buoyancy dominate the θ and S variability. This explains why despite the wind-induced upwelling of warmer subsurface water, steric height has still fallen recently in response to salinity changes.

After all, not all non-seasonal steric height changes can be exclusively attributed to the first two modes. Reconstructing the regional steric height with PC1, PC1+PC2 and PC1+PC2+PC3 with the MLR model shows the compensating or adding behaviour of the second mode and the additional information contained in PC3. As opposed to the subtropical sector, reconstructing the steric height with two modes only does not explain much of the variance of the actual steric height in the subantarctic and the southernmost waters. Here, changes of the third mode explain a considerable part of the remaining steric height variance.
The overall less accurate reconstruction of steric height in the Antarctic sector, even with the added information of all three modes, represents the complexity as well as local differences of the θ and S structure close to the Antarctic coast.

To concisely summarize the regional analysis from a temporal view, it can be said that steric height in the subtropical region has, on average, risen 0.9 cm from 2008 to 2017, mainly as a result of a drastic event of increasing temperature occurring in 2010.
The subantarctic region is subject to an overall freshening, especially in the upper water column from around 1000 m to the surface. Salinity contributes almost as much as temperature to the density anomalies, but there is no significant positive or negative trend in steric height. Steric height in the Antarctic sector has fallen 0.4 cm in the analyzed decade due to a strong increase in salinity since 2014.

5.6 Comparison to altimetry-based SSH

It is now of remaining interest to relate the θ- and S-induced steric height variations to total SLV. Here the zero-centered SSH variability based on satellite observations is directly compared to the above-discussed steric height variability.

The standard deviation of total sea level over the entire Southern Ocean and time period is almost 19 cm higher than that of the steric contribution alone (Table 4.1). While steric height values have a varying range of 2.5 m, SSH ranges significantly more (3.2 m). The mean spatial distribution of total SSH in the Southern Ocean is almost identical to that of steric height, with higher SSH values in the north and and lower values in the south (A.7). The general sea level structure of the present is thus very likely determined by mean variations of θ and S (in the 2000 m column), although there are additional factors that play a role on the mean SSH distribution.

A comparison of the domain mean variations of SSH with steric height over time reveals how seasonal and non-seasonal variability of steric height affected total SLV from 2008 to 2017. Here, another similarity could be identified by comparing the seasonal component of SSH to that of steric height (Figure 5.16).

To exclude that this similarity results from regional differences acting against each other, a seasonal decomposition was performed on the three sectors individually. This confirmed that seasonal fluctuations of SSH and steric height time series are closer correlated in the subtropical and subantarctic sector, and slightly shifted in the Antarctic domain (A.8). The monthly delay of the global domain mean seasonal cycle of steric height is further not exactly equally represented in

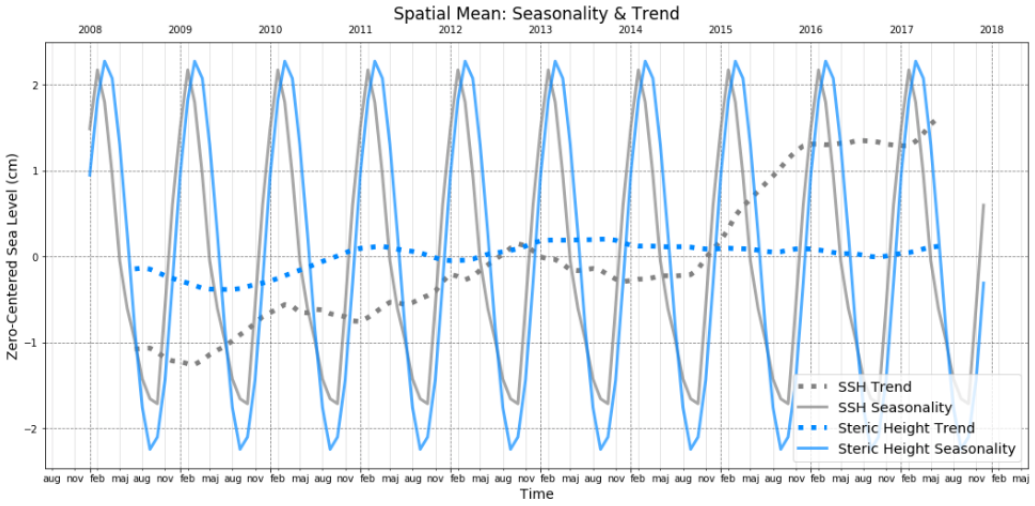

FIGURE (5.16) Trend (dotted lines) and seasonality (solid lines) component of spatial mean SSH and steric height values from 2008 to 2017. Linear steric height trend slope = 0.416 mm/yr with a R^2 = 0.44 (p-value= 0.000). Linear SSH trend slope = 2.954 mm/yr with a R^2 = 0.87 (p-value= 0.000).

the three regions. Steric height in the subantarctic sector has its minimum two months earlier than that revealed by the SSH data from satellite observations, while the maximum corresponds to that of SSH (September). There are also differences in the overall strength of the regional seasonal cycles. Still the seasonal sea level signal in the Southern Ocean is largely affected by θ and S variability.

Since the start of the altimetry era, a common and convenient method to calculate steric height contributions is to subtract the mass component from SSH using gravimetry data (Cazenave and Llovel, 2010; Chambers et al., 2011). Therefore, subtracting the global domain mean steric contribution from that of the SSH data provides information on how the mass component in the Southern Ocean has evolved over the investigated time period.

Indeed the seasonal time series component of the difference portrays a seasonal phenomenon suggested by studies that has been observed globally as well as regionally (Garcia et al., 2007): Steric height reaches its maximum (minimum) shortly before the water budget reaches its minimum (maximum; A.9). Globally, Lombard et al. (2007) detected a 1 to 2 months shift, which is also portrayed herein for the Southern Ocean. This asynchronous occurrence mainly arises due to snow melt during boreal summer (producing barystatic sea level maxima) and heat storage during austral summer (producing steric height maxima; Lombard et al., 2007). This information serves as validation that the difference of investigated SSH and steric height data primarily represents the barystatic component. Seasonal changes of the water budget are thus compensating the thermal expansion maximum in March and

April by -0.5 cm and very likely cause the total intra-annual sea level to drop more rapidly after April.

While seasonal changes of total SSH and steric height both vary on a range of 4 cm, the trend component of the monthly SSH time series is noticeably more linear and accelerating. In the relatively short time period of ten years, the total sea level of the Southern Ocean has risen 3 cm. Only 0.42 cm of this height difference can herewith be explained by an increase in steric height. Although the absolute annual trend of steric height over the investigated period is significantly higher than estimations of earlier studies with comparable time periods until 2015 (Ishii et al., 2006; von Schuckmann et al., 2010; Wang et al., 2017; Storto et al., 2019a), the steric contribution to SLR in the Southern Ocean has decreased significantly. In the study from Storto et al. (2019a) it is already evident that the steric contribution is rapidly decreasing in the later years, as a consequence of increased freshwater discharge. The present study shows that this trend has continued over the recent years, and that despite steric height south of 30°S is more likely to increase than to decrease on average from now on, it is the barystatic contribution that drives present and near future SLR of Southern Ocean waters. The mass input during recent years, mainly from ice sheets and glaciers, has reversed the negative steric height trends in very high latitude waters. Zonal averages of linear trends from 2008 to 2017 suggest annual sea level rises at all latitudes from 0.07 to 0.5 cm per year (Figure 5.17).

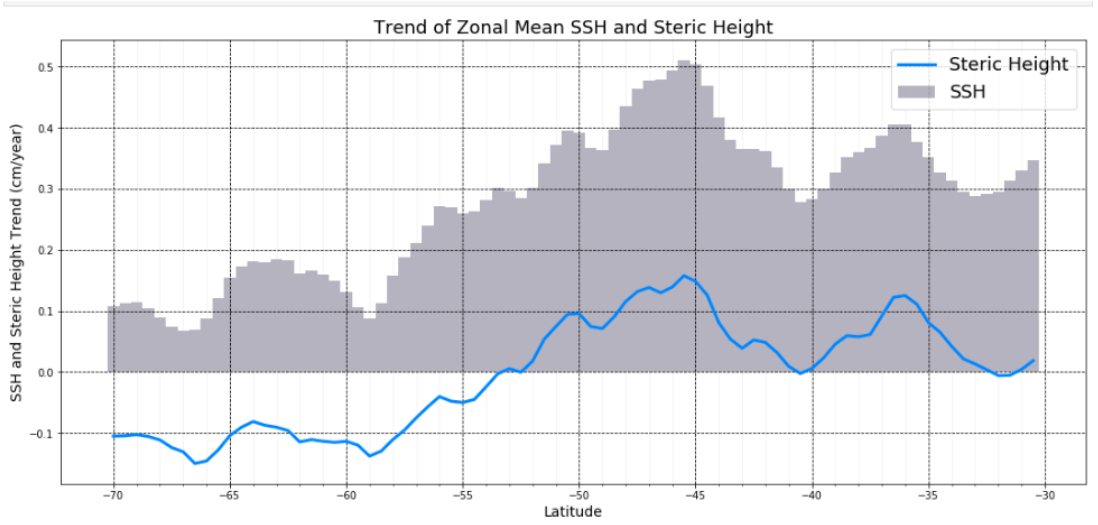

FIGURE (5.17) Linear trend slopes of steric height (blue line) and SSH (grey bars) for every 0.5^{th} latitude from 30°S to 70°S, based on zonal means from 2008 to 2017.

Chapter 6

CONCLUSIONS

The salt and heat content of the Southern Ocean's surface and intermediate layer has increased at nearly all latitudes. The only significant exception occurs in the PFZ, where the surface and intermediate layer has experienced freshening and waters have gotten less warm or have even become slightly colder almost linearly. Especially just north of the STF (35°S to 40°S), there is a strong zonal trend indicating warmer and saltier waters (mainly due to a great increase in 2010). The former cooling of waters close to Antarctica observed in older studies could not be identified. Instead, very high-latitude surface waters are warming at a fast rate since 2014, along with showing higher salt content. Although there are regional disparities at all zonal ranges (see Figure A.4), the overall trend points towards warmer and saltier subtropical, colder and fresher subantarctic, and warmer and saltier Antarctic waters. While higher temperatures north of the ACC portray increased oceanic heat storage from atmospheric warming, the increase in salinity south of the ACC is likely due to increased NADW upwelling as a response to the intensification of westerly winds.

Despite the fact that most regions in the Southern Ocean were subject to higher temperatures, the thermosteric contribution has partly been offset by an increase in salinity. While globally, steric height variability is largely controlled by temperature alone, salinity changes in the Southern Ocean have damped the warming effect south of the PF. This is due to the fact that in the most southern parts of the Southern Ocean, salinity dominates ocean stratification. Even in the subtropical region, it does play a significant role: The freshening of intermediate waters in the vicinity of the Peru current in the South Pacific have counterbalanced the negative steric height trend caused by colder waters (Figure A.4).

Overall, temperature is clearly dominating the present structure and average steric height of the

subtropical waters and further responsible for the positive trend of steric height due to heat storage. It can be concluded that, on average, temperature dominates steric height variability north of the PF, while salinity changes play a vital role south of the PF. As a consequence of an overall increase in temperatures and salinity, steric height has risen in the subtropical waters of the Southern Ocean and has fallen closer to the Antarctic coast.

Steric height changes in the Southern Ocean are significantly affecting total SLV, especially intra-annually. On longer timescales, the rapid rise of total sea level in the Southern Ocean is mainly caused by barystatic processes. From 2008 to 2017, only 7% of total SLR originated from heat and freshwater fluxes. Consistent mass input over the investigated decade has reversed the steric sea level fall near the Antarctic coast and contributed to the steric SLR in subtropical waters of the Southern Ocean.

While steric height levels define intra-annual variations and the average distribution of total SSH over the Southern Ocean, the recent decadal increase (2008 to 2017) was dominantly caused by changes of the global water budget. It is very likely that rising atmospheric temperatures in the following decades will accelerate both the steric and barystatic sea level in the Southern Ocean.

Appendix A

Appendix

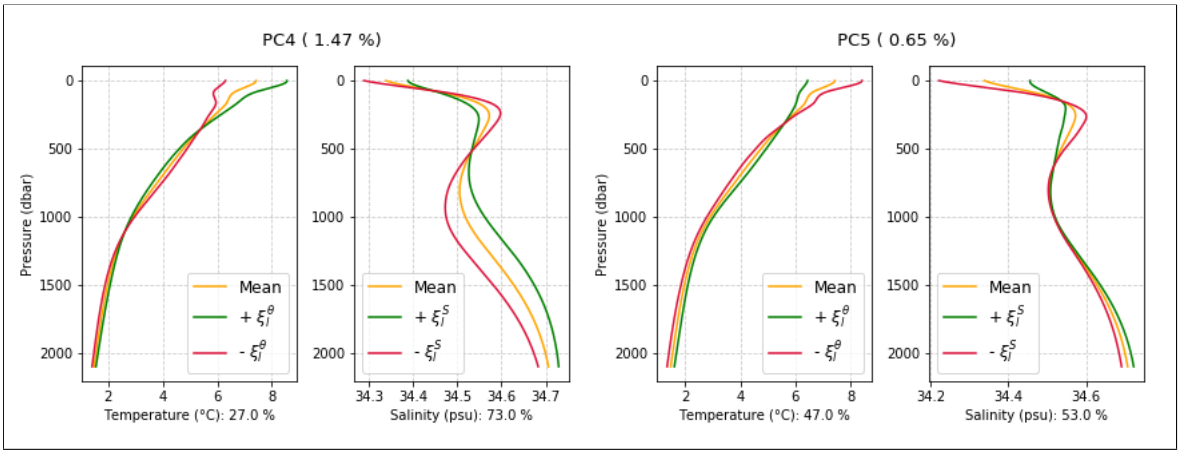

FIGURE (A.1) Effect of adding (green curves) and subtracting (red curves) the eigenfunctions of the mean profiles (yellow curves) computed from the climatology basis.

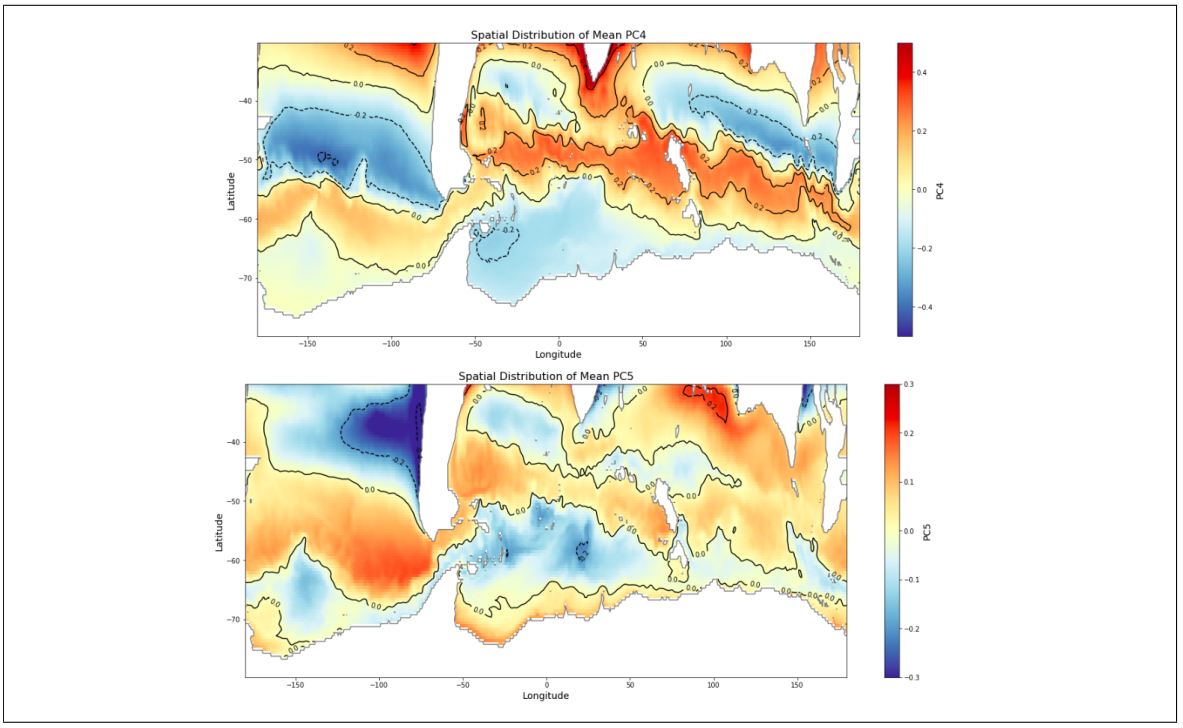

FIGURE (A.2) Spatial distribution of mean PC4 (upper panel) and PC5 (lower panel) from 2008 to 2017 plotted over the entire study domain. Contour Intervals = 0.2 with dashed lines indicating negative values. Adjusted scaling.

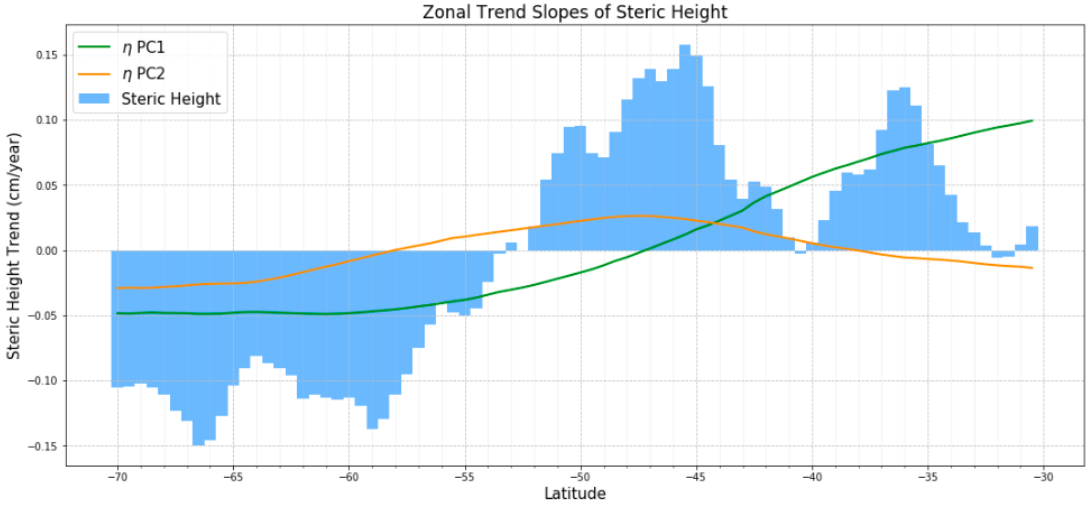

FIGURE (A.3) Linear trend slopes of steric height values for every 0.5^{th} latitude from 30°S to 70°S. Mean effect of PC1 (green line) and PC2 (orange line) on steric height calculated by multiplying the PC values by their regression coefficients (see Table 4.1.)

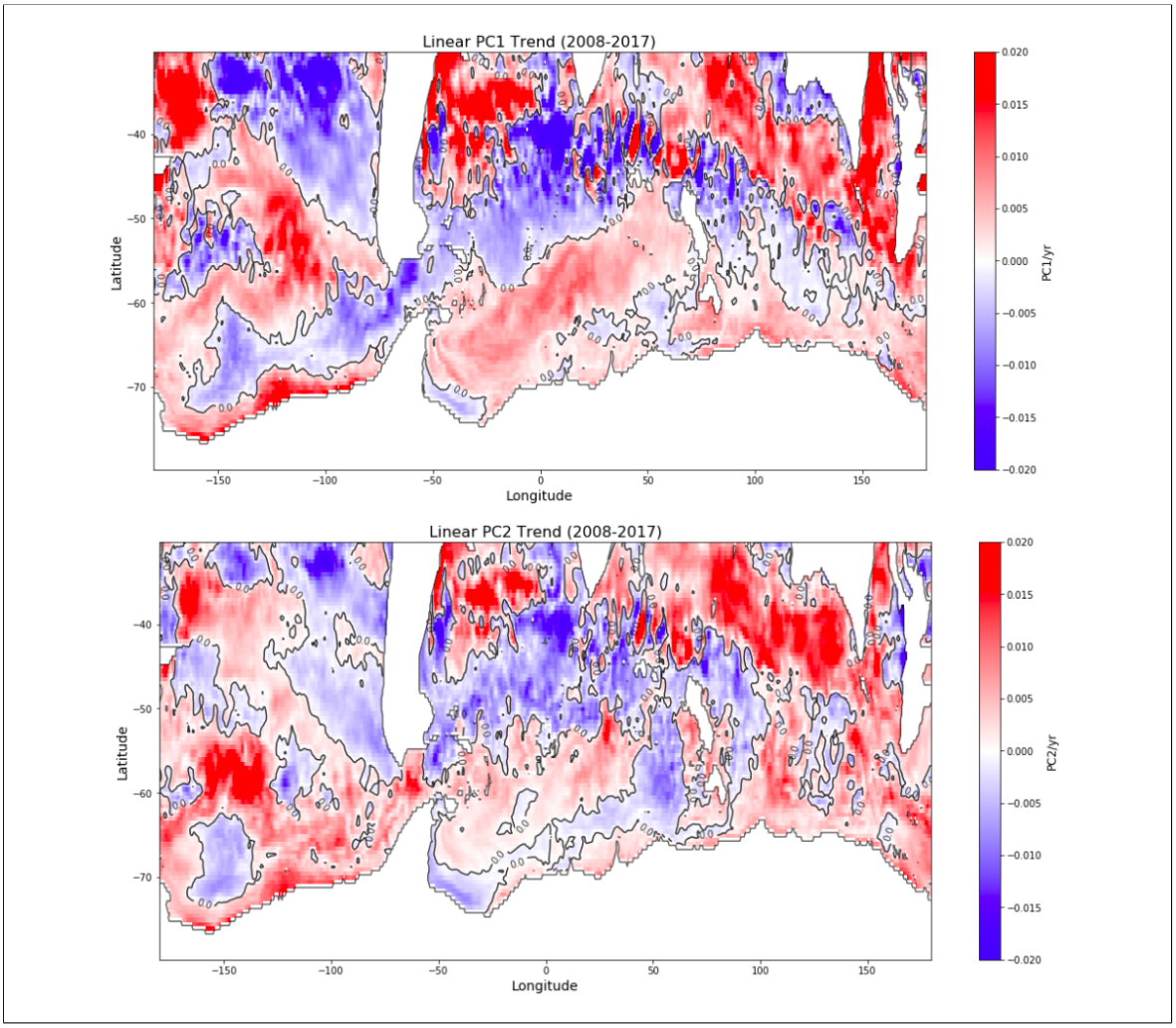

FIGURE (A.4) Map of the PC1 (upper panel) and PC2 (lower panel) trends of steric height per year (from 2008 to 2017) with red colours representing positive and blue colours representing negative linear trend slopes.

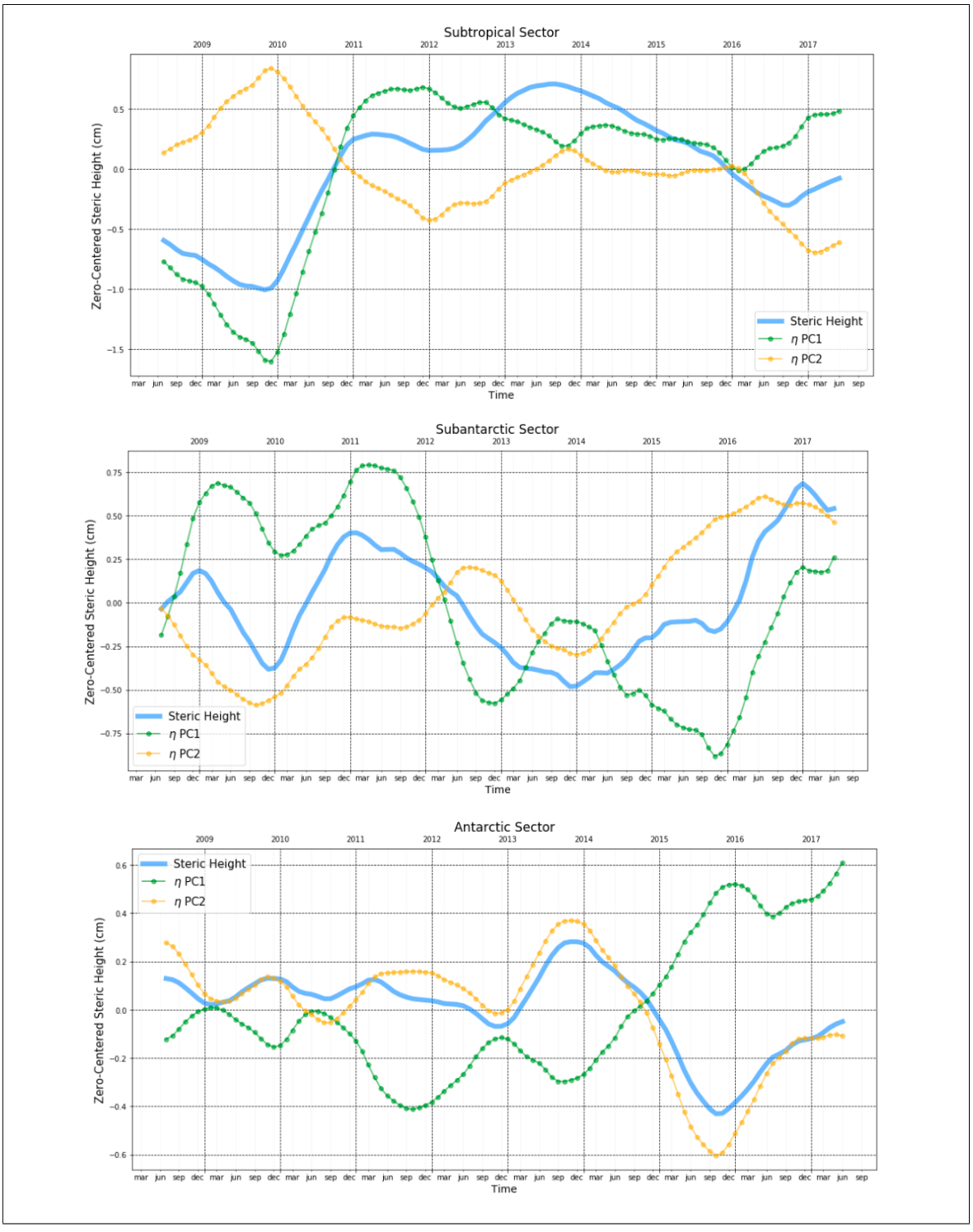

FIGURE (A.5) Seasonally removed monthly time series of steric height contribution of PC1 (dotted green line) and PC2 (dotted orange line), and actual steric height (blue line) in the subtropical (upper panel), the subantarctic (middle panel) and the Antarctic (lower panel) sector from 2008 to 2017.

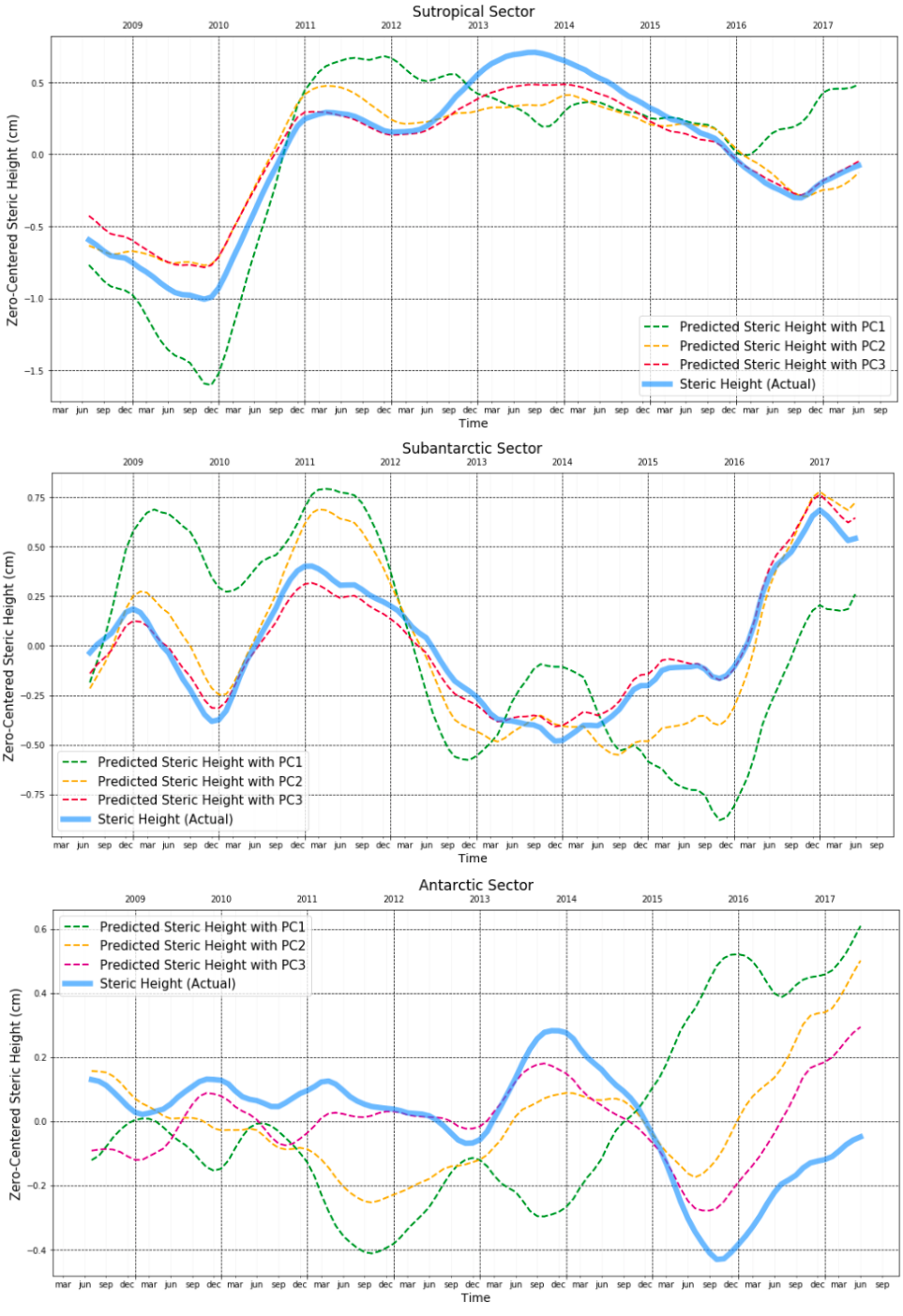

FIGURE (A.6) Seasonally removed monthly time series of reconstructed steric height with PC1 (dashed green line), PC2 (dashed orange line) and PC3 (dashed purple line), and actual steric height (blue line) in the subtropical (upper panel), the subantarctic (middle panel) and the Antarctic (lower panel) sector from 2008 to 2017.

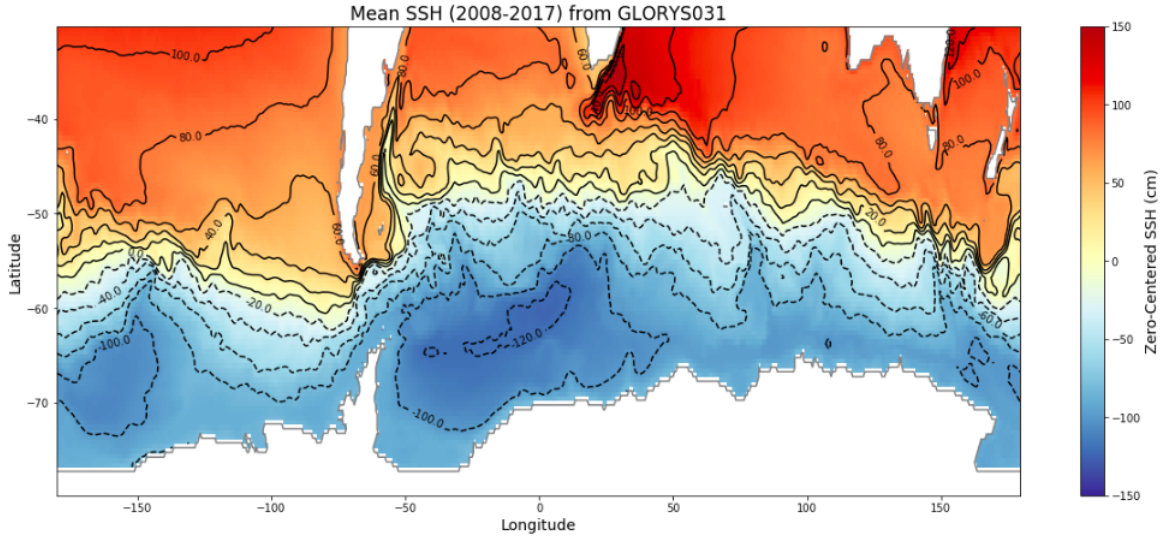

FIGURE (A.7) Map of mean total SSH in cm (2008 to 2017) based on satellite observations (GLORYS031 Ocean Reanalysis).

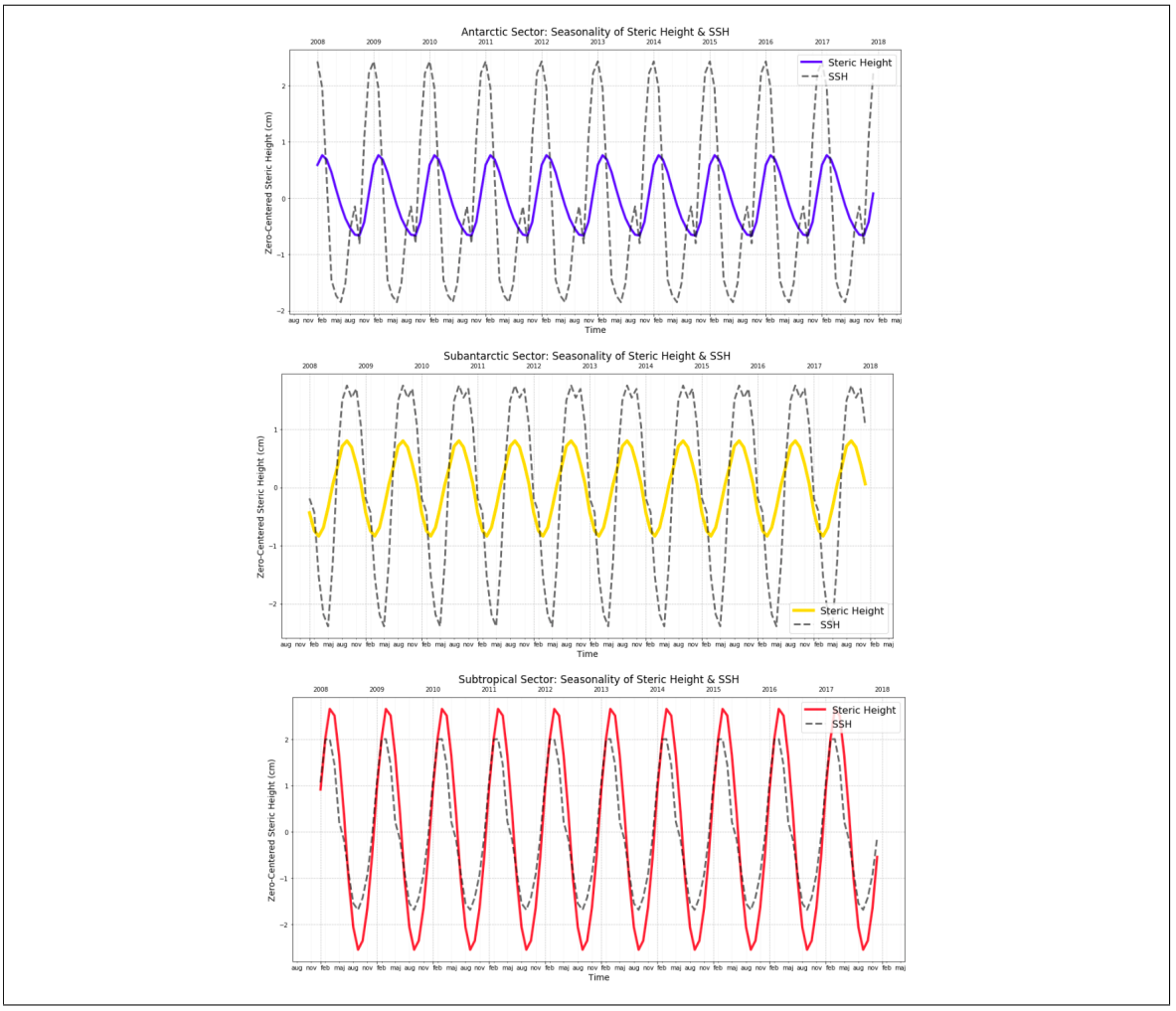

FIGURE (A.8) Seasonal fluctuations of mean steric height (solid lines) and mean SSH (dashed lines) in the subtropical (upper panel), the subantarctic (middle panel) and the Antarctic (lower panel) sector from 2008 to 2017.

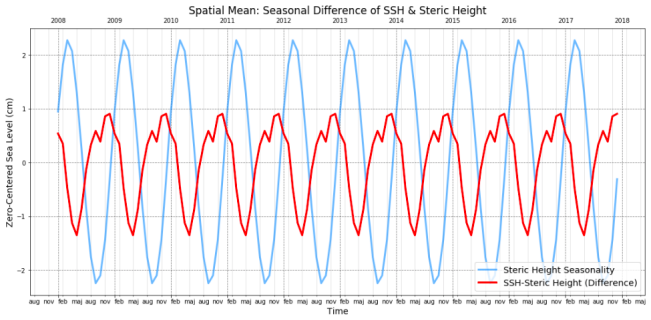

FIGURE (A.9) Seasonal fluctuations of global domain mean steric height (blue line) and the mean difference between SSH and steric height (mass contribution; red line) from 2008 to 2017.

Bibliography

[1] Armitage, T. W., Kwok, R., Thompson, A. F., and Cunningham, G. (2018). Dynamic topography and sea level anomalies of the southern ocean: Variability and teleconnections. *Journal of Geophysical Research: Oceans*, 123(1):613–630.

[2] Armour, K. C., Marshall, J., Scott, J. R., Donohoe, A., and Newsom, E. R. (2016). Southern ocean warming delayed by circumpolar upwelling and equatorward transport. *Nature Geoscience*, 9(7):549–554.

[3] Banerjee, A., Fyfe, J. C., Polvani, L. M., Waugh, D., and Chang, K.-L. (2020). A pause in southern hemisphere circulation trends due to the montreal protocol. *Nature*, 579(7800):544–548.

[4] Belkin, I. M. and Gordon, A. L. (1996). Southern ocean fronts from the greenwich meridian to tasmania. *Journal of Geophysical Research: Oceans*, 101(C2):3675–3696.

[5] Cazenave, A. and Llovel, W. (2010). Contemporary sea level rise. *Annual review of marine science*, 2:145–173.

[6] Chambers, D. P. and Schröter, J. (2011). Measuring ocean mass variability from satellite gravimetry. *Journal of Geodynamics*, 52(5):333–343.

[7] Church, J. A., Clark, P. U., Cazenave, A., Gregory, J. M., Jevrejeva, S., Levermann, A., Merrifield, M. A., Milne, G. A., Nerem, R. S., Nunn, P. D., et al. (2013). Sea level change. Technical report, PM Cambridge University Press.

[8] Clément, L., McDonagh, E. L., Marzocchi, A., and Nurser, A. G. (2020). Signature of ocean warming at the mixed layer base. *Geophysical Research Letters*, 47(1):e2019GL086269.

[9] Collins, M., An, S.-I., Cai, W., Ganachaud, A., Guilyardi, E., Jin, F.-F., Jochum, M., Lengaigne, M., Power, S., Timmermann, A., et al. (2010). The impact of global warming on the tropical pacific ocean and el niño. *Nature Geoscience*, 3(6):391–397.

[10] Constable, A. J., Melbourne-Thomas, J., Corney, S. P., Arrigo, K. R., Barbraud, C., Barnes, D. K., Bindoff, N. L., Boyd, P. W., Brandt, A., Costa, D. P., et al. (2014). Climate change and southern ocean ecosystems i: how changes in physical habitats directly affect marine biota. *Global change biology*, 20(10):3004–3025.

[11] da Gama, V. (2020). Sea-level rise. *Assessment of Climate Change over the Indian Region: A Report of the Ministry of Earth Sciences (MoES), Government of India*, page 175.

[12] Dangendorf, S., Mudersbach, C., Jensen, J., Anette, G., and Heinrich, H. (2013). Seasonal to decadal forcing of high water level percentiles in the german bight throughout the last century. *Ocean Dynamics*, 63(5):533–548.

[13] de Souza, J. M. A. C., Couto, P., Soutelino, R., and Roughan, M. (2020). Evaluation of four global ocean reanalysis products for new zealand waters–a guide for regional ocean modelling. *New Zealand Journal of Marine and Freshwater Research*, pages 1–24.

[14] Donohue, K., Tracey, K., Watts, D., Chidichimo, M. P., and Chereskin, T. (2016). Mean antarctic circumpolar current transport measured in drake passage. *Geophysical Research Letters*, 43(22):11–760.

[15] Farneti, R., Downes, S. M., Griffies, S. M., Marsland, S. J., Behrens, E., Bentsen, M., Bi, D., Biastoch, A., Böning, C., Bozec, A., et al. (2015). An assessment of antarctic circumpolar current and southern ocean meridional overturning circulation during 1958–2007 in a suite of interannual core-ii simulations. *Ocean Modelling*, 93:84–120.

[16] Feucher, C., Maze, G., and Mercier, H. (2019). Subtropical mode water and permanent pycnocline properties in the world ocean. *Journal of Geophysical Research: Oceans*, 124(2):1139–1154.

[17] Freeman, N. M., Lovenduski, N. S., and Gent, P. R. (2016). Temporal variability in the antarctic polar front (2002–2014). *Journal of Geophysical Research: Oceans*, 121(10):7263–7276.

[18] Frölicher, T. L., Sarmiento, J. L., Paynter, D. J., Dunne, J. P., Krasting, J. P., and Winton, M. (2015). Dominance of the southern ocean in anthropogenic carbon and heat uptake in cmip5 models. *Journal of Climate*, 28(2):862–886.

[19] Fukumori, I., Raghunath, R., and Fu, L.-L. (1998). Nature of global large-scale sea level variability in relation to atmospheric forcing: A modeling study. *Journal of Geophysical Research: Oceans*, 103(C3):5493–5512.

[20] Gaillard, F., Reynaud, T., Thierry, V., Kolodziejczyk, N., and Von Schuckmann, K. (2016). In situ–based reanalysis of the global ocean temperature and salinity with isas: Variability of the heat content and steric height. *Journal of Climate*, 29(4):1305–1323.

[21] García, D., Chao, B. F., Del Río, J., Vigo, I., and García-Lafuente, J. (2006). On the steric and mass-induced contributions to the annual sea level variations in the mediterranean sea. *Journal of Geophysical Research: Oceans*, 111(C9).

[22] Garcia, D., Ramillien, G., Lombard, A., and Cazenave, A. (2007). Steric sea-level variations inferred from combined topex/poseidon altimetry and grace gravimetry. In *Deformation and Gravity Change: Indicators of Isostasy, Tectonics, Volcanism, and Climate Change*, pages 721–731. Springer.

[23] Gille, S. T. (2008). Decadal-scale temperature trends in the southern hemisphere ocean. *Journal of Climate*, 21(18):4749–4765.

[24] Gomis, D., Ruiz, S., Sotillo, M. G., Álvarez-Fanjul, E., and Terradas, J. (2008). Low frequency mediterranean sea level variability: the contribution of atmospheric pressure and wind. *Global and Planetary Change*, 63(2-3):215–229.

[25] Goosse, H., Masson-Delmotte, V., Renssen, H., Delmotte, M., Fichefet, T., Morgan, V., Van Ommen, T., Khim, B., and Stenni, B. (2004). A late medieval warm period in the southern ocean as a delayed response to external forcing? *Geophysical Research Letters*, 31(6).

[26] Griggs, G., Cayan, D., Tebaldi, C., Amanda Fricker, H., Arvai, J., DeConto, R., Knopp, R. E., Whiteman, L., Moser, S., and Fox, J. (2017). An update on sea-level rise science. *Rising Seas in California*.

[27] Haid, V., Iovino, D., and Masina, S. (2016). The impact of changes in the antarctic wind field on the southern ocean sea ice. *EGUGA*, pages EPSC2016–15720.

[28] Hallberg, R., Adcroft, A., Dunne, J. P., Krasting, J. P., and Stouffer, R. J. (2013). Sensitivity of twenty-first-century global-mean steric sea level rise to ocean model formulation. *Journal of climate*, 26(9):2947–2956.

[29] Halliwell Jr, G. R. and Allen, J. (1984). Large-scale sea level response to atmospheric forcing along the west coast of north america, summer 1973. *Journal of Physical Oceanography*, 14(5):864–886.

[30] Hellmer, H. H. (2004). Impact of antarctic ice shelf basal melting on sea ice and deep ocean properties. *Geophysical Research Letters*, 31(10).

[31] Ishii, M., Kimoto, M., Sakamoto, K., and Iwasaki, S.-I. (2006). Steric sea level changes estimated from historical ocean subsurface temperature and salinity analyses. *Journal of oceanography*, 62(2):155–170.

[32] Iz, H. B. (2018). The effect of regional sea level atmospheric pressure on sea level variations at globally distributed tide gauge stations with long records. *Journal of Geodetic Science*, 8(1):55–71.

[33] Kim, J.-S., Seo, K.-W., Jeon, T., Chen, J., and Wilson, C. R. (2019). Missing hydrological contribution to sea level rise. *Geophysical Research Letters*, 46(21):12049–12055.

[34] Levitus, S., Antonov, J. I., Boyer, T. P., Baranova, O. K., Garcia, H. E., Locarnini, R. A., Mishonov, A. V., Reagan, J., Seidov, D., Yarosh, E. S., et al. (2012). World ocean heat content and thermosteric sea level change (0-2000 m), 1955–2010. *Geophysical Research Letters*, 39(10).

[35] Li, C., von Storch, J.-S., and Marotzke, J. (2013). Deep-ocean heat uptake and equilibrium climate response. *Climate Dynamics*, 40(5-6):1071–1086.

[36] Liau, J.-R. and Chao, B. F. (2017). Variation of antarctic circumpolar current and its intensification in relation to the southern annular mode detected in the time-variable gravity signals by grace satellite. *Earth, Planets and Space*, 69(1):93.

[37] Llovel, W. and Terray, L. (2016). Observed southern upper-ocean warming over 2005–2014 and associated mechanisms. *Environmental Research Letters*, 11(12):124023.

[38] Lombard, A., Garcia, D., Ramillien, G., Cazenave, A., Biancale, R., Lemoine, J., Flechtner, F., Schmidt, R., and Ishii, M. (2007). Estimation of steric sea level variations from combined grace and jason-1 data. *Earth and Planetary Science Letters*, 254(1-2):194–202.

[39] Madec, G., Bourdallé-Badie, R., Bouttier, P.-A., Bricaud, C., Bruciaferri, D., Calvert, D., Chanut, J., Clementi, E., Coward, A., Delrosso, D., et al. (2017). Nemo ocean engine.

[40] Milne, G. A., Gehrels, W. R., Hughes, C. W., and Tamisiea, M. E. (2009). Identifying the causes of sea-level change. *Nature Geoscience*, 2(7):471–478.

[41] Nagura, M. and McPhaden, M. J. (2018). The shallow overturning circulation in the indian ocean. *Journal of Physical Oceanography*, 48(2):413–434.

[42] NAS Ocean Studies and National Academies of Sciences, Engineering, and Medicine and others (2017). *Antarctic Sea Ice Variability in the Southern Ocean-Climate System*. National Academies Press.

[43] Nerem, R. S., Beckley, B. D., Fasullo, J. T., Hamlington, B. D., Masters, D., and Mitchum, G. T. (2018). Climate-change–driven accelerated sea-level rise detected in the altimeter era. *Proceedings of the National Academy of Sciences*, 115(9):2022–2025.

[44] Newman, L., Heil, P., Trebilco, R., Katsumata, K., Constable, A., van Wijk, E., Assmann, K., Beja, J., Bricher, P., Coleman, R., et al. (2019). Delivering sustained, coordinated, and integrated observations of the southern ocean for global impact. *Frontiers in Marine Science*, 6:433.

[45] Nghiem, S., Rigor, I., Clemente-Colón, P., Neumann, G., and Li, P. (2016). Geophysical constraints on the antarctic sea ice cover. *Remote sensing of Environment*, 181:281–292.

[46] Orsi, A. H., Whitworth III, T., and Nowlin Jr, W. D. (1995). On the meridional extent and fronts of the antarctic circumpolar current. *Deep Sea Research Part I: Oceanographic Research Papers*, 42(5):641–673.

[47] Pauthenet, E., Roquet, F., Madec, G., and Nerini, D. (2017). A linear decomposition of the southern ocean thermohaline structure. *Journal of Physical Oceanography*, 47(1):29–47.

[48] Pauthenet, É., Roquet, F., Madec, G., Sallée, J.-B., and Nerini, D. (2019). The thermohaline modes of the global ocean. *Journal of Physical Oceanography*, 49(10):2535–2552.

[49] Pellichero, V., Sallée, J.-B., Schmidtko, S., Roquet, F., and Charrassin, J.-B. (2017). The ocean mixed layer under southern ocean sea-ice: Seasonal cycle and forcing. *Journal of Geophysical Research: Oceans*, 122(2):1608–1633.

[50] Pollard, R., Lucas, M., and Read, J. (2002). Physical controls on biogeochemical zonation in the southern ocean. *Deep Sea Research Part II: Topical Studies in Oceanography*, 49(16):3289–3305.

[51] Pond, S. and Pickard, G. L. (1983). *Introductory dynamical oceanography*. Gulf Professional Publishing.

[52] Ponte, R. M. (2006). Low-frequency sea level variability and the inverted barometer effect. *Journal of Atmospheric and Oceanic Technology*, 23(4):619–629.

[53] Ramsay, J. O. (2004). Functional data analysis. *Encyclopedia of Statistical Sciences*, 4.

[54] Ramsay, J. O. and Silverman, B. W. (2007). *Applied functional data analysis: methods and case studies*. Springer.

[55] Rintoul, S. R. and Sokolov, S. (2001). Baroclinic transport variability of the antarctic circumpolar current south of australia (woce repeat section sr3). *Journal of Geophysical Research: Oceans*, 106(C2):2815–2832.

[56] Riser, S. C., Freeland, H. J., Roemmich, D., Wijffels, S., Troisi, A., Belbéoch, M., Gilbert, D., Xu, J., Pouliquen, S., Thresher, A., et al. (2016). Fifteen years of ocean observations with the global argo array. *Nature Climate Change*, 6(2):145–153.

[57] Roemmich, D., Alford, M. H., Claustre, H., Johnson, K. S., King, B., Moum, J., Oke, P. R., Owens, W. B., Pouliquen, S., Purkey, S., et al. (2019). On the future of argo: A global, full-depth, multi-disciplinary array. *Frontiers in Marine Science*, 6:439.

[58] Sallée, J.-B., Shuckburgh, E., Bruneau, N., Meijers, A. J., Bracegirdle, T. J., and Wang, Z. (2013). Assessment of southern ocean mixed-layer depths in cmip5 models: Historical bias and forcing response. *Journal of Geophysical Research: Oceans*, 118(4):1845–1862.

[59] Scott, M. (2019). Antarctica is colder than the arctic, but it's still losing ice.

[60] Shi, J.-R., Talley, L. D., Xie, S.-P., Liu, W., and Gille, S. T. (2020). Effects of buoyancy and wind forcing on southern ocean climate change. *Journal of Climate*, pages 1–53.

[61] Silva, N., Rojas, N., and Fedele, A. (2009). Water masses in the humboldt current system: Properties, distribution, and the nitrate deficit as a chemical water mass tracer for equatorial subsurface water off chile. *Deep Sea Research Part II: Topical Studies in Oceanography*, 56(16):1004–1020.

[62] Skinner, L., Menviel, L., Broadfield, L., Gottschalk, J., and Greaves, M. (2020). Southern ocean convection amplified past antarctic warming and atmospheric co 2 rise during heinrich stadial 4. *Communications Earth & Environment*, 1(1):1–8.

[63] Sokolov, S. and Rintoul, S. R. (2009). Circumpolar structure and distribution of the antarctic circumpolar current fronts: 2. variability and relationship to sea surface height. *Journal of Geophysical Research: Oceans*, 114(C11).

[64] Stammer, D. and Cazenave, A. (2017). *Satellite altimetry over oceans and land surfaces*. CRC Press.

[65] Stammer, D., Cazenave, A., Ponte, R. M., and Tamisiea, M. E. (2013). Causes for contemporary regional sea level changes. *Annual review of marine science*, 5:21–46.

[66] Stocker, T. F., Qin, D., Plattner, G.-K., Tignor, M., Allen, S. K., Boschung, J., Nauels, A., Xia, Y., Bex, V., Midgley, P. M., et al. (2013). Climate change 2013: The physical science basis. *Contribution of working group I to the fifth assessment report of the intergovernmental panel on climate change*, 1535.

[67] Storto, A., Bonaduce, A., Feng, X., and Yang, C. (2019a). Steric sea level changes from ocean reanalyses at global and regional scales. *Water*, 11(10):1987.

[68] Storto, A., Masina, S., Simoncelli, S., Iovino, D., Cipollone, A., Drevillon, M., Drillet, Y., von Schuckmann, K., Parent, L., Garric, G., et al. (2019b). The added value of the multi-system spread information for ocean heat content and steric sea level investigations in the cmems grep ensemble reanalysis product. *Climate dynamics*, 53(1-2):287–312.

[69] Sun, C. and Watts, D. R. (2002). Heat flux carried by the antarctic circumpolar current mean flow. *Journal of Geophysical Research: Oceans*, 107(C9):2–1.

[70] Sutton, P. and Roemmich, D. (2011). Decadal steric and sea surface height changes in the southern hemisphere. *Geophysical research letters*, 38(8).

[71] Tamisiea, M. E. and Mitrovica, J. X. (2011). The moving boundaries of sea level change: Understanding the origins of geographic variability. *Oceanography*, 24(2):24–39.

[72] Tsimplis, M. N., Marcos, M., and Somot, S. (2008). 21st century mediterranean sea level rise: steric and atmospheric pressure contributions from a regional model. *Global and Planetary Change*, 63(2-3):105–111.

[73] Viviani, R., Grön, G., and Spitzer, M. (2005). Functional principal component analysis of fmri data. *Human brain mapping*, 24(2):109–129.

[74] von Schuckmann, K., Speich, S., Gaillard, F., and Le Traon, P.-Y. (2010). Large regional contributions of ocean heat content variability, freshwater content and steric height changes. *EGUGA*, page 11888.

[75] Wang, G., Cheng, L., Boyer, T., and Li, C. (2017). Halosteric sea level changes during the argo era. *Water*, 9(7):484.

[76] Weisstein, E. W. (2009). Bézier curve. *MathWorld—A Wolfram Web Resource*.

[77] Wijffels, S., Roemmich, D., Monselesan, D., Church, J., and Gilson, J. (2016). Ocean temperatures chronicle the ongoing warming of earth. *Nature Climate Change*, 6(2):116–118.

[78] Wu, L., Jing, Z., Riser, S., and Visbeck, M. (2011). Seasonal and spatial variations of southern ocean diapycnal mixing from argo profiling floats. *Nature Geoscience*, 4(6):363–366.

[79] Zhang, L., Delworth, T. L., Cooke, W., and Yang, X. (2019). Natural variability of southern ocean convection as a driver of observed climate trends. *Nature Climate Change*, 9(1):59–65.